Long-term sub-micron aerosol chemical composition in the boreal forest: inter- and intra-annual variability

Liine Heikkinen[1], Mikko Äijälä[1], Matthieu Riva[1,2], Krista Luoma[1], Kaspar Dällenbach[1], Juho Aalto[3], Pasi Aalto[1], Diego Aliaga[1], Minna Aurela[4], Helmi Keskinen[1], Ulla Makkonen[4], Pekka Rantala[1], Markku Kulmala[1], Tuukka Petäjä[1], Douglas Worsnop[1,5], and Mikael Ehn[1]

[1]Institute for Atmospheric and Earth System Research /Physics, Faculty of Science, University of Helsinki, Helsinki, FI–00014, Finland
[2]Univ Lyon, Université Claude Bernard Lyon 1, CNRS, IRCELYON, 69626, Villeurbanne, France
[3]Institute for Atmospheric and Earth System Research /Forest Sciences, Faculty of Agriculture and Forestry, University of Helsinki, Helsinki, FI–00014, Finland
[4]Atmospheric Composition Research, Finnish Meteorological Institute, Helsinki, FI–00101, Finland
[5]Aerodyne Research Inc., Billerica, MA, USA

Correspondence to: Liine Heikkinen (liine.heikkinen@helsinki.fi) and Mikael Ehn (mikael.ehn@helsinki.fi)

Abstract.

The Station for Measuring Ecosystem Atmosphere Relations (SMEAR) II is well known among atmospheric scientists due to the immense amount of observational data it provides of the earth–atmosphere interface. Moreover, SMEAR II plays an important role in large European research infrastructures, enabling the large scientific community to tackle climate and air pollution related questions, utilising the high-quality long-term data sets recorded at the site. So far, the well-documented site was missing the description of the seasonal variation of aerosol chemical composition that is crucial for understanding the complex biogeochemical and -physical processes governing the forest ecosystem. Here, we report the sub-micron aerosol chemical composition and its variability utilising data measured between 2012 and 2018 using an Aerosol Chemical Speciation Monitor (ACSM). We observed a bimodal seasonal trend in the sub–micron aerosol concentration culminating in February (2.7, 1.6, 5.1 µg m^{-3} for median, 25th, 75th percentiles, respectively) and July (4.2, 2.2, and 5.7 µg m^{-3} for median, 25th, 75th percentiles, respectively). The wintertime maximum was linked to an enhanced presence of inorganic aerosol species (ca. 50%) whereas the summertime maximum (ca. 80% organics) to biogenic secondary organic aerosol (SOA) formation. During the exceptionally hot Julys of 2014 and 2018, the organic aerosol concentrations were up to 70% higher than the 7–year July mean. The projected increase of heat wave frequency over Finland will most likely influence the loading and chemical composition of aerosol particles in the future. Our findings suggest strong influence of meteorological conditions such as radiation, ambient temperature, wind speed and direction on aerosol chemical composition. To our understanding, this is the longest time series reported describing the aerosol chemical composition measured online in the boreal region, but the continuous monitoring will be maintained also in the future.

1 Introduction

Both climate change and air pollution represent global grand challenges. Detailed monitoring of environments showing vulnerability towards them is crucial. The arctic and boreal forest are examples of such regions (Prăvălie, 2018;Kulmala, 2018). The boreal forest represents ~15% of the Earth's terrestrial area, spanning between 45 and 70 °N, and making up ~ 30% of the world's forests (Prăvălie, 2018). Over the course of the predicted warming, the boreal forest is likely to

move further north, resulting in arctic greening. In addition, the presence of southerly tree species are projected to increase in the southern regions of the biome (Settele et al., 2014). These large–scale changes are linked to numerous complex biogeochemical and -physical processes. These complexities greatly hamper our ability to make detailed predictions of future changes, as exemplified by diversities in global model outputs of many important ecosystem- and climate-relevant parameters (Fanourgakis et al., 2019). To help improve and constrain modelling efforts, comprehensive long-term high-quality observational data are of utmost importance (Kulmala, 2018). Among the important parameters to monitor, atmospheric composition, including both gaseous and particulate matter, provides a crucial link between the ecosystems and climate.

Atmospheric aerosol particles affect Earth's radiative balance, influence ecosystems and human health, and reduce visibility (Ramanathan et al., 2001;Boucher et al., 2013;Myhre et al., 2013). These particles can be emitted directly into the atmosphere or form through gas-to-particle transition reactions from atmospheric vapours (Kulmala et al., 2004). The composition of atmospheric aerosol particles has an extensive degree of variability depending on their origin. Their composition covers a wide range of organic and inorganic species with differing physicochemical properties. These properties affect the aerosol-related disturbances on the Earth's radiative forcing as salt particles scatter radiation efficiently, whereas soot particles absorb it. In addition to this direct radiative effect, aerosol particles also participate in cloud formation and processing. Indeed, every cloud droplet forms from an aerosol particle seed, termed a cloud condensation nucleus (CCN). Moreover, these cloud seeds are often hygroscopic, which is directly linked to their chemical composition. Important contributors to discrepancies estimating aerosol sensitivity of the boreal climate are challenges in reproducing observations of aerosol chemical composition and properties (Fanourgakis et al., 2019).

Solar radiation and ambient temperature control both biogenic and human (anthropogenic) behaviour. In the northern latitudes, the amount of radiation varies considerably in the course of a year yielding a large seasonal variation in ambient temperature. The ambient temperature also fluctuates notably in diurnal scale. Ambient temperature influences emissions of various biogenic volatile organic compounds (BVOCs) including monoterpenes (Guenther et al., 1993), whereas solar radiation enables the photochemical reactions leading to oxidation products having lower volatilities. Secondary organic aerosol (SOA) is formed from the partitioning of oxidised VOCs to the condensed phase. SOA is a key component in tropospheric PM worldwide (Zhang et al., 2007a;Jimenez et al., 2009). While warmer conditions promote the emissions of BVOCs, cold temperatures enhance the need of residential heating leading to emissions of primary particles as well as a large variety of anthropogenic trace gases.

The major inorganic sub-micron aerosol species, of which the majority also originate from anthropogenic activities, are sulphate, nitrate and ammonium (Zhang et al., 2007b;Jimenez et al., 2009). The presence of sulphur dioxide (SO_2), emitted to the atmosphere from industrial processes and volcanic activity, has significantly increased compared to pre-industrial conditions (Tsigaridis et al., 2006). It forms sulphuric acid upon oxidation that besides participating in the formation of new particles, also readily condenses onto pre–existing aerosol particles increasing the particle mass loading and ultimately modifying the acidity of atmospheric particles. Ammonia (NH_3), emitted in large quantities from industry and agriculture, can partly neutralise particulate sulphuric acid forming ammonium sulphate, acknowledged as one of the main contributors to sub–micron aerosol mass. In addition, ammonium nitrate, formed from the reaction between ammonia and nitric acid is a common inorganic PM constituent. Nitrogen oxides (NO_x = NO + NO_2) from traffic

emissions and industry are the major nitric acid precursors in the atmosphere. These radicals play an important role in atmospheric chemistry due to their high reactivity.

The concentrations of primary aerosol particles and the aerosol precursors (such as NO_x, NH_3, SO_2, and (B)VOCs) vary during the year especially in the northern latitudes, where temperature differences between summer and winter are drastic. Besides differences in the emissions, also the dynamics (thickness) of the atmospheric boundary layer influences airborne pollutant concentrations. For example, during sunny summer days the boundary layer height can exceed two kilometres height in the Northern hemisphere (McGrath-Spangler and Denning, 2013), and emissions from the surface are widely dispersed in a large volume. During wintertime, the boundary layer can be more than a kilometre shallower than in summer, and the pollutant loadings become concentrated closer to the surface. The boundary layer thickness is determined by atmospheric stability. In unstable conditions, the air is rising and well mixed due to heating from below. In stable conditions, generally caused by cooling from below, turbulence is supressed and mixing occurs only close to the Earth's surface. Shallow, nocturnal boundary layers are often stable due to radiative cooling from the Earth's surface.

To conclude, the aerosol chemical composition and loading in the lower troposphere are highly dependent on different emission sources and meteorological conditions. As these vary over the course of a year, also seasonal variation can be expected in aerosol composition and loading. Importantly, variation also occurs invariably in inter–annual scale. For example, year–to–year variation in ambient temperature is normal, but expected to increase with increased frequency of climate extremes introduced by climate change (Pachauri and Meyer, 2014;Kim et al., 2018). Such variations could affect air pollutant loadings in the boreal region, as milder winters might lead to a decrease of emissions from domestic wood burning, and warmer summers might enhance the emissions from frequent and intense wild fires as well as promote SOA formation from oxidised BVOCs. Inter–annual variability in aerosol composition and loading can also be introduced by emission regulations. For example, atmospheric PM_{10}, $PM_{2.5}$, SO_2 and NO_x concentrations have shown decreasing trends in the past decades in United States and Europe (Wang et al., 2012;Aas et al., 2019;Anttila and Tuovinen, 2010;Simon et al., 2014). Hence, for a well representative overview of aerosol climatology, and to truly capture seasonal variations regarding air pollutants in the ruling boreal climate, a long–enough time series is required for analysis. Only then, a good overview can be given of trends, variability, and seasonal and diurnal cycles of aerosol concentrations and composition.

The current study focuses on the seasonal variation of aerosol chemical composition and its year-to-year fluctuation at the Station for Measuring Ecosystem – Atmosphere relations (SMEAR) II (Hari and Kulmala, 2005), located in the boreal forest of Finland. The measurement period spans over seven years. SMEAR II is well known for its comprehensive, simultaneous measurements tracking >1000 different environmental parameters within the Earth–atmosphere interface covering forest, wetland and lake areas (Hari and Kulmala, 2005). Furthermore, SMEAR II is part of large research networks such as Aerosols, Clouds and TRace gases InfraStructure (ACTRIS), Integrated Carbon Observation System (ICOS), Europe's Long–term Ecosystem Research (LTER) and the infrastructure for Analysis and Experimentation on Ecosystems (AnaEE).

The chemical composition of aerosol particles at SMEAR II has been studied previously in multiple short (<1 – 10 month) measurement campaigns with both offline (Saarikoski et al., 2005;Kourtchev et al., 2005;Cavalli et al., 2006;Finessi et al., 2012;Corrigan et al., 2013;Kourtchev et al., 2013;Kortelainen et al., 2017), and online methods (Allan et al.,

2006;Finessi et al., 2012;Häkkinen et al., 2012;Corrigan et al., 2013;Crippa et al., 2014;Hong et al., 2014;Makkonen et al., 2014;Äijälä et al., 2017;Hong et al., 2017;Kortelainen et al., 2017;Riva et al., 2019;Äijälä et al., 2019). The previous studies include several important discoveries regarding SMEAR II aerosol composition. For example, a large mass fraction of particulate matter has been found to be (oxidised) organic aerosol (Corrigan et al., 2013;Crippa et al., 2014;Äijälä et al., 2017;Äijälä et al., 2019), and recognised as terpene oxidation products (Kourtchev et al., 2005;Allan et al., 2006;Cavalli et al., 2006;Finessi et al., 2012;Corrigan et al., 2013;Kourtchev et al., 2013). In addition to this forest-generated SOA, a nearby sawmill also contributes significantly to the OA loading in the case of south easterly winds (e.g. Liao et al., 2011;Corrigan et al., 2013;Äijälä et al., 2017). The composition of the sawmill-OA is found to significantly resemble biogenic OA (Äijälä et al., 2017). Also biomass burning organic aerosol (BBOA) contributes to the OA mass (Corrigan et al., 2013; Crippa et al., 2014; Äijälä et al., 2017; Äijälä et al., 2019). The BBOA presence in the summertime aerosol depends on long-range transport of wildfire plumes. Inorganic species from anthropogenic activities, majority identified as ammonium sulphate and nitrate, are also transported to the station. Ammonium sulphate represents the dominating inorganic species (e.g. Saarikoski et al., 2005; Äijälä et al., 2019). Despite the long list of studies and discoveries, the measurement/sampling periods have occurred mostly between early spring and late autumn, leaving the description of the wintertime aerosol composition nearly fully lacking. Hence, based on these studies alone, the understanding of the degree of variability in aerosol chemical composition at SMEAR II is incomplete – in both intra- and inter-annual scales.

Here, we provide a comprehensive overview of sub-micron aerosol chemical composition at SMEAR II. This study does not only provide the analysis of the longest time series of sub–micron aerosol chemical composition measured on–line in the climate–sensitive boreal environment, but also introduces the data set to the scientific community for further utilisation with other SMEAR II, ACTRIS, ICOS, LTER and AnaEE data to improve our understanding of the aerosol sensitivity of the (boreal) climate.

2 Measurements and methods

In this chapter, we introduce the SMEAR II measurement site, data processing and analysis tools. As the meteorological conditions ruling at the station are of high importance influencing sub-micron aerosol chemical composition, we will first focus on giving an overview of the SMEAR II climate. The instrument operation, data processing and analysis part briefly describes the instrumentation used, focusing mainly on the aerosol chemical speciation monitor (ACSM) that serves as the key instrument for the current study.

2.1 SMEAR II description

The measurements reported here were conducted at the SMEAR II station (61°51’N, 24°17’E, 181 m above sea level) (Hari and Kulmala, 2005) between years 2012 and 2018. However, they continue also after 2018 as part of the station’s long-term measurements. SMEAR II is located in a nearly 60-year-old Scots pine (Pinus sylvestris) dominated stand. A previous land use survey reveals that a majority of the area surrounding the station is forested, as 80% of the land within 5 km radius and 65% within 50 km radius is covered by mixed forest (Williams et al., 2011). The forested area located north west of the station is shown to have least anthropogenic air pollutant sources (Williams et al., 2011;Tunved et al., 2006). However, 90% of the forests in Fennoscandia region are introduced to anthropogenic influence via forest management (Gauthier et al., 2015). The city of Tampere (population approximately 235 000) lies within the 50 km radius

to the south west introducing a notable source of anthropogenic pollution. Other evident nearby sources of anthropogenic pollution are the town of Orivesi (population approximately 9 200) 19 km south of SMEAR II and the nearby village of Korkeakoski with two saw mills and a pellet factory 6–7 km to the south east from SMEAR II (Liao et al., 2011;Äijälä et al., 2017). Nonetheless, the dominating source of air pollutants are air masses advected from industrialized areas over southern Finland, St. Petersburg region in Russia and continental Europe (Kulmala et al., 2000;Patokoski et al., 2015;Riuttanen et al., 2013). The anthropogenic emissions are minor at the station. Monoterpenes, notably α–pinene and Δ^3–carene, are the dominating emitted biogenic non–methane VOCs from the forest (Hakola et al., 2012;Barreira et al., 2017).

The mean annual temperature at the measurement station during the measurement period (2012–2018), recorded at 4.2 m above ground level, was 5.4 °C. In average, January was the coldest month (T_{avg} = –6.2 °C) and July the warmest (T_{avg} = 16.6 °C). The mean annual temperature recorded was ca. 2°C higher than the 1981–2010 annual mean reported (Pirinen et al., 2012). The seasonal and diurnal variation of temperature is presented in Figure 1a followed by the corresponding data for global radiation above the forest (Figure 1b). November and December were the darkest months whereas the radiation maximum was reached in late May and early June, which is earlier than generally observed at the top of the atmosphere. The reason for the early radiation maximum peaking time is the increased fractional cloud cover in July (Tuononen et al., 2019), likely promoted by convection. The formation of convective clouds hinders the transmission of solar radiation to the lower troposphere, and increases the intensity of precipitation, making the 1981–2010 mean precipitation maximum occur in July (92 mm) (Pirinen et al., 2012). However, November, December and January hold the greatest amount of precipitation days (≥ 0.1 mm for ca. 21 days per month). The annual 1981–2010 mean cumulative precipitation is 711 mm (Pirinen et al., 2012). The first snow on the ground can be expected in November, and the snow depth maximum is commonly reached in March. The snow cover is roughly lost in April (Pirinen et al., 2012). The wind direction recorded above the forest canopy during the measurement period is normally from the south west with enhanced southerly influence during winter months (especially in January and February) and has large scatter during summer months (Figure 1c&Figure A.1a-c). The diurnal mean of wind speeds above the forest canopy were usually greatest during wintertime as can be expected based on overall Northern hemispheric behaviour. The seasonal cycles of wind speed show most diurnal variability from May to September (Figure 1d&Figure A.1a-c).

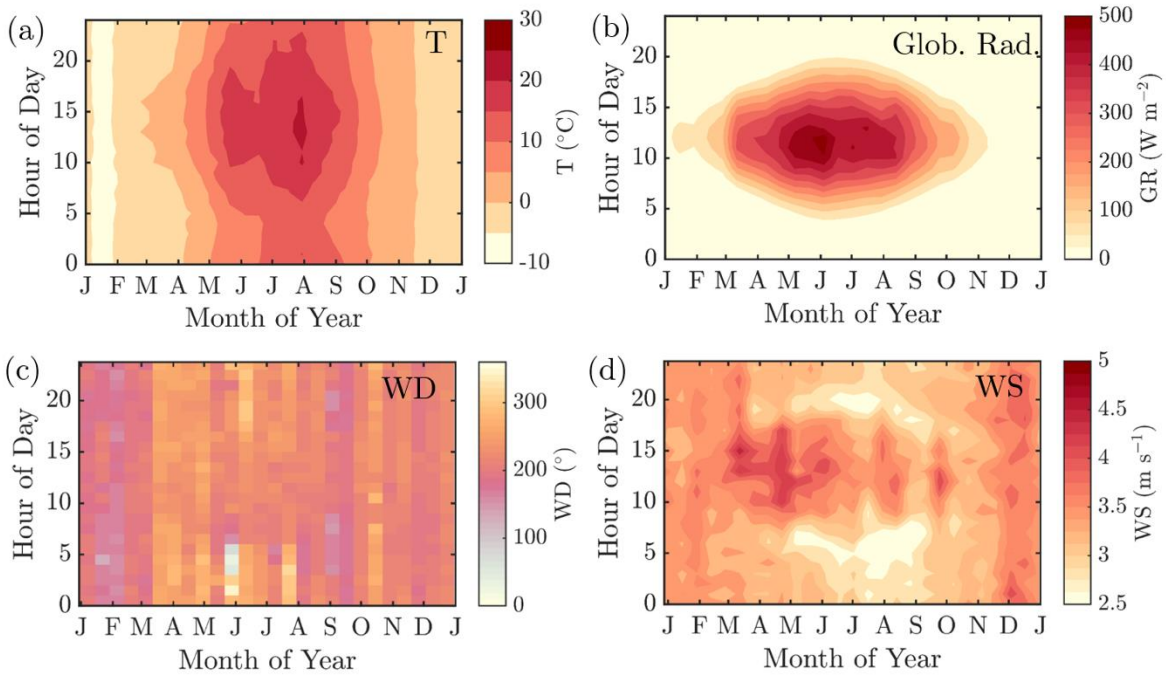

184

185 **Figure 1** The seasonal evolution of diurnal cycles of ambient temperature measured 4.2 m above ground level (panel a), global
186 radiation above the forest canopy (panel b), wind direction above the forest canopy (panel c), and wind speed above the forest canopy
187 (panel d) recorded at SMEAR II station in 2012 – 2018. The y–axes in the figures represent the local time of day (UTC+2) and the x–
188 axes the time of the year. The colour scales correspond to the temperature in degrees Celsius, global radiation in W m^{-2}, wind direction
189 in degrees and wind speed in m s^{-1}, respectively. Panels a, b and d include interpolation of the 14 d × 1 h resolution data grid into
190 isolines based on the MATLAB2017a *contourf* function. Panel c has no interpolation involved due to challenges related to interpolating
191 over a circularly behaving variable. The plot is produced with MATLAB 2017a *pcolor* function.

192

193 **2.2 ACSM measurements**

194 The Aerosol Chemical Speciation Monitor (ACSM; Aerodyne Research Inc. USA) was first described by Ng et al. in
195 2011. It was developed based on the Aerosol Mass Spectrometer (AMS) (Canagaratna et al., 2007), but simplified at the
196 cost of mass and time resolution to achieve a robust instrument for long–term measurements. The ACSM samples ambient
197 air with a flow rate of 1.4 cm^3 s^{-1} through a critical orifice (100 µm in diameter) towards an aerodynamic lens efficiently
198 transmitting particles between approximately 75 and 650 nm in vacuum aerodynamic diameter (D_{va}) and pass through
199 particles further up to 1µm in D_{va} with a less efficient transmission (Liu et al., 2007). After this, the particles are flash
200 vaporized at a 600 °C hot surface in high vacuum and ionised with electrons from a tungsten filament (70 eV, electron
201 impact ionisation, EI). These processes lead to substantial fragmentation of the molecules forming the aerosol particles.
202 The resulting ions are guided to a mass analyser, a residual gas analyser (RGA) quadrupole, scanning through different
203 mass–to–charge ratios (*m/Q*). The detector is a secondary electron multiplier (SEM). The particulate matter detected by
204 the ACSM is referred to as non–refractory (NR) sub–micron particulate matter (PM_1). The word 'non–refractory' (NR)
205 is attributed to the instrument limitation to detect material flash evaporating at 600 °C thus being unable to measure heat–
206 resistant material such as minerals or soot. The word 'PM_1' is linked to the aerodynamic lens approximate cut-off at 1
207 µm. Importantly, the NR–PM_1 reported from these ACSM measurements is a difference between the signal of particle-
208 laden air and signal recorded when the sampling flow passed a particle filter (filtered air).

The ACSM measurements for the current study were conducted within the forest canopy through the roof of an air conditioned container. A $PM_{2.5}$ cyclone was used to filter out big particles that could cause clogging of the critical orifice. A Nafion dryer was installed in 2013 upstream the instrument ensuring a sampling relative humidity (RH) below 30%. Before this, the RH was not controlled nor recorded. Thus, the RH was likely high during summer, but low during wintertime. Moreover, a 3 litres per minute (Lpm) overflow, which was ejected only before the aerodynamic lens, was used to minimise losses in the sampling line (length approximately 3 m). The data were acquired using the ACSM data acquisition software (DAQ) provided by Aerodyne Research Inc., the instrument manufacturer. The DAQ version was updated upon new releases. The ACSM was operated to perform *m/Q* scans with a 200 ms Th^{-1} scan rate in the mass–to–charge range of *m/Q* 10 Th to 140 Th. Filtered and particle–laden air were measured interchangeably for 28 quadrupole scans resulting in ca. 30 minute averages. The air signal, obtained from the automatic filter measurements, was subtracted from the sample raw signal, yielding the signal from aerosol mass only. The data processing was performed using ACSM Local v. 1.6.0.3 toolkit within the Igor Pro v. 6.37 (Wavemetrics Inc., USA). Upon data processing, the different detected ions were assigned into organic or inorganic species bins (i.e. total organics, sulphate, nitrate, ammonium and chloride) using a fragmentation table (Allan et al., 2004). Moreover, the data were normalized to account for N_2 signal variations related to ACSM flow rate and sensitivity changes (due to SEM voltage response decay).

The ACSM raw signal (IC) is converted to mass concentration (*C*) with the following equation obtained from Ng et al. (2011):

$$C_{\mathrm{s}} = \frac{1}{\mathrm{CE} \times \frac{T_m}{Q}} \times \frac{10^{12}}{\mathrm{RIE_s} \times \mathrm{RF_{NO_3}}} \times \frac{Q_{\mathrm{cal}} \times G_{\mathrm{cal}}}{Q \times G} \times \sum_{i=0}^{n} \mathrm{IC}_{s,i}, \quad (1)$$

where C_s is the concentration of species *s*, CE is the particle collection efficiency (see chapter 2.4 ACSM collection efficiency correction), and $T_{m/Q}$ the *m/Q* –dependent ion transmission efficiency in the RGA quadrupole mass analyser. The $T_{m/Q}$ is constantly recorded based on naphthalene fragmentation patterns and their comparison to naphthalene fragmentation pattern in the NIST data base (75 eV EI; http://webbook.nist.gov/). Naphthalene is used as an internal standard in the ACSM and is thus always present in the mass spectrum (Ng et al., 2011). The RIE_s is the relative ionisation efficiency of species *s* and RF_{NO_3} the ACSM response factor determined through ionisation efficiency (IE) calibrations with ammonium nitrate (NH_4NO_3). The RF_{NO_3} explains the ACSM ion signal (A) per µg m^{-3} of nitrate. Q_{cal} and G_{cal} are the ACSM volumetric flow rate and detector gain during ACSM calibration, whereas *Q* and *G* are the values during the measurement period for volumetric flow rate and detector gain, respectively. They generally correspond the calibration values. The final parameter is the sum of the signal introduced by individual ions ($IC_{s,i}$) originating from species *s*.

The ionisation efficiency calibration was performed with dried and size–selected ammonium nitrate (NH_4NO_3) particles to retrieve the RF_{NO_3} parameter required in Equation (1). In addition, ammonium sulphate ($(NH_4)_2SO_4$) calibrations were carried out, albeit less frequently, providing a value for the sulphate relative ionization efficiency (RIE_{SO_4}). RIE_{NH_4} was derived from the ammonium nitrate calibration. Constant RF and RIE values were used for each year, respectively. The conversion from ACSM raw signal to mass concentration was performed with the ACSM Local v. 1.6.0.3 provided by Aerodyne Research Inc.

2.3. Additional measurements

In addition to the ACSM–measurements, the SMEAR II station has a large number of other air composition related measurements. In the current study, we investigate only a small fraction of them. The particle measurements (i.e. ACSM, Differential Mobility Particle Sizer (DMPS), Dekati cascade impactor, Aethalometer, Organic Carbon and Elemental Carbon (OCEC) analyser and Monitor for AeRosols and Gases in ambient Air (MARGA) 2S) were conducted in two measurement containers and a cabin, all located within ca. 50 m from each other. The gas phase sampling of NO_x, SO_2, CO and VOCs as well as temperature, wind and global radiation measurements, were conducted from the station mast that has several measurement heights from near ground to 127 m height. The temperature measurement was conducted with a Pt100 sensor (4.2 m above ground level), the global shortwave radiation with a Middleton SK08 pyranometer (125 m above ground level). The horizontal wind measurements were conducted with Thies 2D Ultrasonic anemometers above the forest canopy (16.8 to 67.2 m above ground level). The NO_x measurements were performed with a TEI 42 iTL chemiluminescence analyser equipped with a photolytic Blue Light Converter ($NO_2^{\bullet}$ to $NO^{\bullet}$) converter, SO_2 with a TEI 43 iTLE fluorescence analyser, and CO with IR absorption analysers Horiba APMA 370 (until January 2016) and API 300EU (from February 2016 onwards). The NO_x, SO_2, CO and PTR–MS sampling was conducted 67.2 m above ground level. The SO_2, NO_x, CO, and PTR–MS (only 2012–2013), and meteorology data were uploaded from Smart–SMEAR data base (https://avaa.tdata.fi/web/smart) (Junninen et al., 2009). The DMPS, Dekati impactor, Aethalometer, OCEC–analyser and MARGA–2S measurements were conducted within the forest canopy are described in more detail in the sections below. The data availability is shown in Figure A.2.

2.3.1 DMPS

The Differential Mobility Particle Sizer (DMPS) measures the aerosol size distribution below 1 µm electrical mobility diameter. SMEAR II holds the world record in online aerosol size distribution measurements (Dada et al., 2017), as the measurements started already in 1996. The DMPS system is described in detail previously (Aalto et al., 2001). Briefly, the SMEAR II DMPS is a twin DMPS setup that samples 8 m above ground from an inlet with a flow rate of 150 Lpm. The measurement cycle is 10 minutes. The first DMPS (DMPS–1) has a 10.9 cm long Vienna type differential mobility analyser (DMA) and a model TSI3025 condensation particle counter (CPC) that was changed to model TSI3776 after October 2016. The sheath flow rate in the DMA is 20 Lpm and aerosol flow rate 4.0 Lpm. The measurement range of the DMPS–1 is 3–40 nm. The second DMPS (DMPS–2) has a 28 cm long Vienna type DMA and a TSI3772 CPC. The sheath flow rate is 5 Lpm and the aerosol flow rate 1 Lpm. The measurement range is 20 nm – 1 µm. The sheath flows are dried (RH < 40%), and controlled with regulating valves as well as measured with TSI mass flow meters operated in volumetric flow mode. The aerosol flow is brought to charge balance with 370 MBq C–14, and after March 2018 with a 370 MBq Ni–63 radioactive beta source. The aerosol flow rates are monitored with pressure drop flow meters. The aerosol flows were not dried. Temperatures and RHs are monitored from DMPS excess flow and from the aerosol inlet. The aerosol flow rates were checked and adjusted every week against a Gilian Gilibrator flow meter throughout the measurement period. The DMA high voltages were also validated with a multimeter. The CPC concentrations were compared against each other with size–selected ammonium sulphate particles in the 6–40 nm range as well as compared against the TSI3775 particle counter that measures the total aerosol particle number concentration at the station. The sizing accuracy of the two DMAs were cross-compared with 20 nm ammonium sulphate particles. In addition, the accuracies of the RH, temperature and pressure probes were validated each year.

2.3.2 Cascade impactor

The PM_1 and $PM_{2.5}$ (particulate mass of aerosol particles with an aerodynamic diameter below 2.5 µm) mass concentrations measured between 2012–2017, which were included in the current study, were retrieved from the cascade impactor measurements. This gravimetric PM_{10} impactor, produced by Dekati Ltd., is a three–stage impactor with cut–points at 10, 2.5 and 1 µm. The collection is conducted on greased (Apiezon vacuum grease diluted in toluene) Nuclepore 800 203 25 mm polycarbonate membranes with 30 Lpm flow rate, approximately 5 m above ground level. The filter smearing was performed to avoid losses due to particle bouncing. The filters were weighed manually every 2–3 days and stored in a freezer for possible further analysis.

2.3.3 PTR–MS

The monoterpene concentration was measured using the proton transfer reaction quadrupole mass spectrometer (PTR–MS) manufactured by Ionicon Analytik GmbH, Innsbruck, Austria (Lindinger and Jordan, 1998). The monoterpene measurement setup is described in detail previously (Rantala et al., 2015). Shortly, the PTR–MS was placed inside a measurement cabin on the ground level and the sample air was drawn down from a measurement mast to the instrument using a 157 m long PTFE tubing (16/14 mm o.d./i.d.). The sampling line was heated and the sample flow was 45 Lpm. However, the sample entering the PTR–MS was only 0.1 Lpm. During the study period, the primary ion signal H_3O^+ (measured at isotope *m/Q* 21 Th) varied slightly around 5–30 × 10^6 c.p.s. (counts per seconds). The instrument was calibrated every 2–4 weeks using three different VOC standards (Aper–Riemer) and the instrumental background was measured every third hour using VOC free air, produced by a zero air generator (Parker ChromGas, model 3501). Normalised sensitivities and the volume mixing ratios were then calculated using the method introduced previously (Taipale et al., 2008). For example, the normalized sensitivity of alpha–pinene (measured at *m/Q* 137 Th) varied between 2 and 5 n.c.p.s. p.p.b.$^{-1}$ over the study period. Only the signal of monoterpenes at *m/Q* 137 Th were analysed in the current study.

2.3.4 Aethalometer

The concentration of equivalent black carbon (eBC) in the PM_1 size range was measured by using two different Magee Scientific Aethalometer models: AE–31 during 2012–2017, and AE–33 in 2018. The sample air was taken through an inlet equipped with a PM_{10} cyclone and a Nafion dryer, and a PM_1 impactor. Aethalometers determine the concentration of eBC by collecting aerosols on a filter medium and measuring the change in light attenuation trough the filter. Both of the Aethalometers quantify eBC concentration optically at seven wavelengths (370, 470, 520, 590, 660, 880 and 950 nm). Only the eBC concetration determined at 880 nm was used in the current study. AE–31 data was corrected for a filter loading error with a correction algorithm derived previously (Collaud Coen et al., 2013). A mass absorption cross section of 4.78 m^2 g^{-1} at 880 nm was used in the eBC concentration calculation. The AE–33 used a "dual–spot" correction is described previously (Drinovec et al., 2015).

2.3.5 OCEC–analyser

Organic carbon (OC) and elemental carbon (EC) concentrations were measured using a semi–continuous Sunset OCEC analyser (Bauer et al., 2009) produced by Sunset Laboratories Inc. (USA). The aerosol sampling was conducted through the same container roof as the ACSM. The inlet length was approximately the same as for the ACSM (ca. 3 m). The sample flow was guided through a $PM_{2.5}$ cyclone and a carbon plate denuder to avoid collection of large particles and a

positive artefact introduced by organic vapours. In the OCEC, the sample is collected on a quartz–filter for 2.5 hours with an 8 Lpm flow rate. The sampling procedure is followed by the analysis phase. The analysis phase includes thermal desorption of PM from the filter following the EUSAAR–2 protocol (Cavalli et al., 2010), and introducing the aerosol sample to inert helium gas that is used to carry the OC to a MnO_2 oxidising oven. This leads to OC oxidation to CO_2, which is then quantified, with a non–dispersive infrared (NDIR) detector. Afterwards the remaining sample is introduced to a mixture of oxygen and helium enabling EC transfer to the oven. The resulting CO_2 from EC desorption and combustion is also quantified using the NDIR detector. An additional optical correction was used to account for the amount of pyrolysed OC during the helium phase. EC was also quantified using a laser installed in the analyser. This method is similar to the Aethalometer (see chapter 2.3.4 Aethalometer). After each analysis phase, a calibration cycle was performed via methane oxidation. The instrument was maintained extensively in November 2017, thus making the year 2018 most reliable for ACSM comparison. Only data measured in 2018 was used in this study.

2.3.6 MARGA–2S

Inorganic gases (HCl, HNO_3, HONO, NH_3, SO_2) and major inorganic ions in $PM_{2.5}$ and PM_{10} fraction (Cl^-, NO_3^-, SO_4^{2-}, NH_4^+, Na^+, K^+, Mg^{2+}, Ca^{2+}) were measured with one hour time–resolution using the online ion chromatograph MARGA 2S ADI 2080 (Applikon Analytical BV, Netherlands). In the MARGA instrument, ambient air was taken through the inlet to a wet rotating denuder where the gases were diffused in absorption solution (10 p.p.m hydrogen peroxide). Aerosol particles that passed through denuder were collected in a steam jet aerosol collector. The sample solutions from the denuder as well as the steam jet aerosol collector were collected in syringes and injected in an anion and cation ion chromatograph with an internal standard solution (LiBr). Cations were separated in a Metrosep C4 (100/4.0) cation column using 3.2 mmol L^{-1} MSA eluent. For anions, a Metrosep A Supp 10 (75/4.0) column with Na_2CO_3 – $NaHCO_3$ (7 mmol L^{-1} / 8 mmol L^{-1}) eluent were used. The detection limits for all the components were 0.1 µg m^{-3}, or smaller. The unit used for the current study is described in more detail previously (Makkonen et al., 2012).

2.4 ACSM collection efficiency correction

The ACSM data processing includes correcting for the measurement collection efficiency (CE) that is estimated to be approximately 0.45–0.5 in average for AMS-type instruments (Middlebrook et al., 2012). The reduction is caused by particle bouncing at the instrument vaporizer (Middlebrook et al., 2012). Middlebrook et al. (2012) provide a method to estimate the CE, based on aerosol chemical composition. However, this method was not applicable to our data set due to low, and thus noisy, ammonium signals that were most of the time near the instrument detection limit. Thus, we chose to calculate the collection efficiency based on the ratio between the NR–PM_1 (total mass concentration measured by the ACSM) and a Differential Mobility Particle Sizer (DMPS)–derived mass concentration (after subtracting the equivalent black carbon, eBC). The DMPS-derived mass concentration is determined as follows: 1) Calculation of aerosol volume concentration (m^3 m^{-3}) of the ACSM detectable size range, where the aerodynamics lens transmission is most efficient (50–450 nm in electrical mobility = ~75–650 nm in vacuum aerodynamic diameter) and assuming spherical particles, 2) Estimating aerosol density based on the ACSM-measured chemical composition ($\rho_{(NH_4)_2SO_4}$= 1.77 g cm^{-3}, $\rho_{NH_4NO_3}$= 1.72 g cm^{-3}, ρ_{Org}= 1.50 g cm^{-3}, ρ_{BC} = 1.00 g cm^{-3}), 3) Calculating the mass concentration (µg m^{-3}; mass concentration = density × volume concentration). As direct scaling of ACSM data to the DMPS-derived and eBC subtracted mass concentration is strongly not recommended, we chose to use two-month running medians of the ratio between the NR–PM_1 and eBC-subtracted DMPS-derived mass concentration. The two–month running median approach diminishes the effect instrument

noise in the DMPS–derived mass concentration that could otherwise be introduced as additional uncertainty into the ACSM–data. The two-month median CEs were within 10% of the annual mean values in years 2013–2018. In 2012 the CE had stronger seasonal variation (16% variation around the mean, peaking in summer) likely due to the lack of the aerosol dryer in the sampling line. The magnitudes of the CEs can be obtained from Figure 2a.

Figure 2a depicts the linear regression fits for ACSM mass concentration (without CE correction) and eBC–subtracted DMPS–derived mass concentration scatter plots for each year. The correlation coefficients (Pearson R^2) between these two independently measured variables are high, indicating that both ACSM and DMPS functioned well throughout the long dataset. Years 2012, 2016–2018 have linear regression fit slopes (k) corresponding to CE values reported in the literature (Middlebrook et al., 2012), whereas slopes for years 2013–2015 were higher than expected. The most likely reason for these high values were calibration difficulties that might have led to underestimation of the instrument RF_{NO_3} that is required in the mass concentration calculation. This possible RF_{NO_3} underestimation was accounted for in the DMPS–based CE correction with higher CE values than theoretically suggested for ACSM–systems. The resulting agreement between the eBC–subtracted DMPS–derived mass concentration and the CE corrected ACSM–derived mass concentration is presented in Figure 2b. As the NR–PM_1 incorporates the two–month running median of the CE calculated using DMPS–data, it is not surprising that a good correlation was achieved.

Figures 2c&d visualise the relationship between ACSM–derived mass concentration and a Dekati impactor PM_1 data (see 2.3.2 Cascade impactor for instrument description) before and after CE correction, respectively. The impactor PM_1 is not eBC subtracted as it would have significantly decreased the number of points in the analysis. The degree of agreement between the ACSM and impactor measurements is significantly lower compared to the agreement between the ACSM and DMPS. The reason for this is likely the fact that the Dekati impactor measurements are prone to uncertainties due to long sampling times and manual weighing. This scatter is reduced slightly in Figure 2d compared to Figure 2c due to the DMPS–based CE correction and the slope–values (k) increase. As the agreement between the ACSM–derived mass concentration and impactor PM_1 is better after CE correction both due to increased correlation coefficients (R^2) and slopes (k), the (two month running median) DMPS–based CE correction is justified. Hereafter, all the ACSM data presented and discussed are CE corrected. We refer to it as NR–PM_1. The CE correction method applied importantly also ensures more quantitative year-to-year comparability of the ACSM data acquired as it also corrected for the overestimated calibration values obtained during 2013–2015.

2.5 ACSM chemical speciation validation

To validate the ACSM chemical speciation process, the ACSM organics (Org) and sulphate (SO_4) were compared against the organic carbon (OC) measured by a Sunset OCEC–analyser (see section 2.3.5 OCEC-analyser for instrument) (Figure 2e) and water-soluble sulphate measured by a MARGA–2S (see section 2.3.5 MARGA-2S for instrument description) (Figure 2f), respectively. Both of these reference instruments sample the $PM_{2.5}$ range, and thus we expect them to detect also larger particles and thus a higher mass loading than the ACSM, when particles exceeding 1 µm in aerodynamic diameter are present in the ambient air. The OC and Org measurements show a high degree of agreement indicated by Pearson R^2 of 0.72 during the overlapping measurement period at SMEAR II. The slope of the linear regression fit (k = 1.52) is comparable to literature values of organic matter to organic carbon ratios (OM:OC) (Turpin and Lim, 2001;Lim and Turpin, 2002;Russell, 2003). The linear regression is calculated using all the overlapping data from year 2018, when

the OCEC was well functioning after instrument service. Regarding the water-soluble inorganic ions, only the SO_4^{2-} concentration (in $PM_{2.5}$), retrieved from the MARGA measurements, was used for the current analysis for ACSM data validation purposes. The nitrate time series, for example, are known to be different between the two measurements at SMEAR II (Makkonen et al., 2014). The scatter between the nitrate measurements, visualised also here, in Figure A.3, could serve as evidence of organic nitrates, which are not efficiently detected by MARGA (Makkonen et al., 2014). The presence of organic nitrates are discussed later in the manuscript (see chapter 3.2 Diurnal variation of NR–PM_1 composition). Other factors influencing the nitrate agreement could arise from the MARGA nitrate background subtraction procedure, the overall low nitrate signal at SMEAR II (Makkonen et al., 2014), an organic CH_2O^+ fragment coinciding with NO^+ at *m/Q* 30 Th leading to ACSM nitrate over prediction under certain conditions, and the difference between the ACSM and MARGA size cuts (PM_1 vs $PM_{2.5}$). The ACSM sulphate, however, correlates well with MARGA (Pearson $R^2 = 0.77$), but has a slightly lower Pearson R^2 compared to an earlier < 11–month MARGA vs AMS comparison from SMEAR II (Pearson $R^2 = 0.91$) (Makkonen et al., 2014). Overall, based on the good agreement between ACSM and Sunset OCEC, MARGA, DMPS and Dekati cascade impactor measurements, we are confident of the year–to–year comparability of our ACSM dataset.

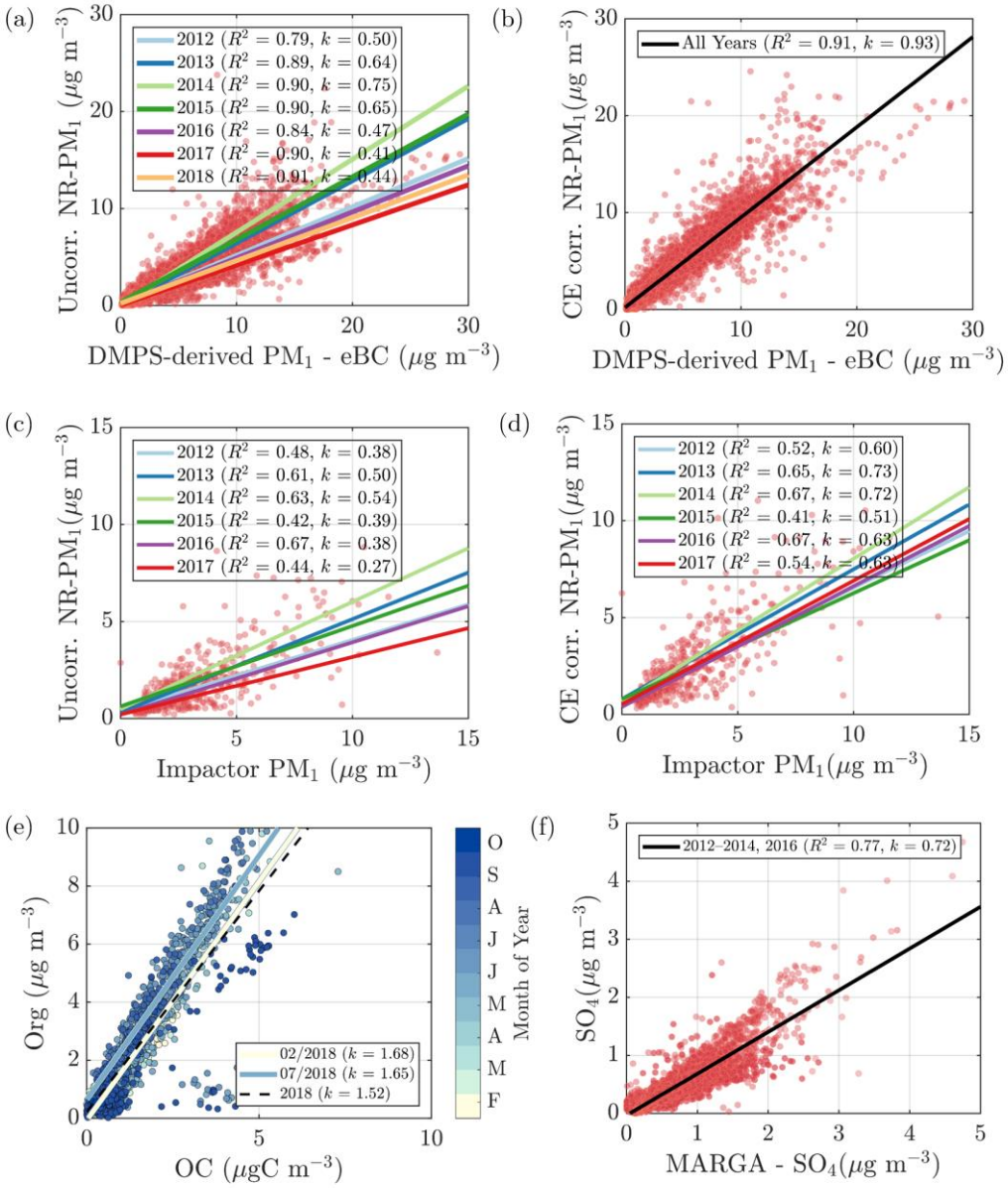

Figure 2 (Panel a) The NR–PM$_1$ mass concentration without collection efficiency (CE) correction vs the DMPS–derived eBC subtracted mass concentration. The linear fits are displayed with solid lines for each year, respectively. The slopes of the linear fits (k) and Pearson correlation coefficients (R^2) are presented in the figure legend. (Panel b) CE–corrected NR–PM$_1$ mass concentration vs the DMPS–derived eBC subtracted mass concentration. The black line represents the overall linear fit. (Panel c) The NR–PM$_1$ mass concentration without collection efficiency (CE) correction vs the Dekati impactor PM$_1$ concentration. The linear fits are displayed with solid lines for each year, respectively. (Panel d) CE–corrected NR–PM$_1$ mass concentration vs correction vs the Dekati impactor PM$_1$ concentration. The linear fits are displayed with solid lines for each year, respectively. (Panel e) The ACSM organics vs the PM$_{2.5}$ organic carbon (OC) detected with a semi–continuous OC/EC analyser. The black dashed line represents the overall linear fit (Pearson R^2 = 0.72), and the solid white and blue linear fit lines represent the February and July fits, respectively. The color coding indicates the month of the year in 2018. (Panel f) The ACSM sulphate vs the PM$_{2.5}$ sulphate detected with MARGA–2S. The black line represents the overall linear fit. In all of the panels, red dots represent all the measurement points collected in the course of the measurement period.

2.6 Openair polar plots with ZeFir pollution tracker

The wind direction dependence of different NR–PM_1 chemical species observed at SMEAR II were investigated with openair bivariate polar plots. Openair is an open source, R–based package described previously (Carslaw and Ropkins, 2012). Briefly, the openair polar plots show how the pollutant concentration varies under different wind speed and direction. The calculation of the polar plots are based on binning pollutant concentration data into different wind direction and speed bins followed by the concentration field interpolation. As the polar plots do not take the frequencies of the wind direction nor wind speed into account, they should be investigated together with a traditional wind rose representing the likelihood of each wind direction and wind speed combination. The ZeFir pollution tracker (Petit et al., 2017), an Igor Pro (Wavemetrics Inc, USA) based graphical interface for producing openair polar plots among other functionalities, was utilized in the current study. Median statistics with fine resolution were set in the ZeFir–based openair initialisation. These plots provide an informative first step for tracking PM_1 and its precursors' wind direction and speed dependence.

3 Results and discussion

First, we state that the ACSM data set was not long enough to provide sufficient statistics for investigation of long–term trends of NR–PM_1 or its components' loading, hence no analysis of such is presented here. In this section we discuss the inter– and intra–annual variation in sub–micron non–refractory aerosol chemical composition at SMEAR II in 2012–2018. We first introduce the monthly scale behaviour and year–to–year variability. We briefly introduce two case studies, one linked to elevated sulphate loading at the station due to a lava field eruption in Iceland, and another one discussing the effect of heatwaves on PM_1 loading and composition. Hereafter, we introduce the overall median diurnal profiles of individual chemical species observed in the NR–PM_1, and finally the chemical composition observations linked to wind speed and direction observations above the forest canopy.

3.1 Inter– and intra–annual variation

The monthly median seasonal cycles of NR–PM_1 and $PM_{2.5}$ show bimodal distributions as the PM loading has two maxima: one peak in February, and another one in summer (June, July, and August), the latter one being more significant. This can be observed from Figures 3a&b, where the monthly median PM loading for each year is visualised. The NR–PM_1 seasonal cycle (Figure 3a) is more pronounced compared to the $PM_{2.5}$ cycle (Figure 3b). A possible reason for this could be the lack of $PM_{2.5}$ data in 2018 that is having a high impact on the NR–PM_1 July peak. The $PM_1/PM_{2.5}$ ratio (Figure 3c) in turn, calculated using the Dekati Impactor data alone, demonstrates that most of the time, 60–80% of $PM_{2.5}$ can be explained by PM_1. The ratio is lowest (60–70%) in wintertime (December, January, February) implying an increased mass fraction of particles with aerodynamic diameters greater than a micrometre, compared to the summertime, when the ratio is nearly 80%.

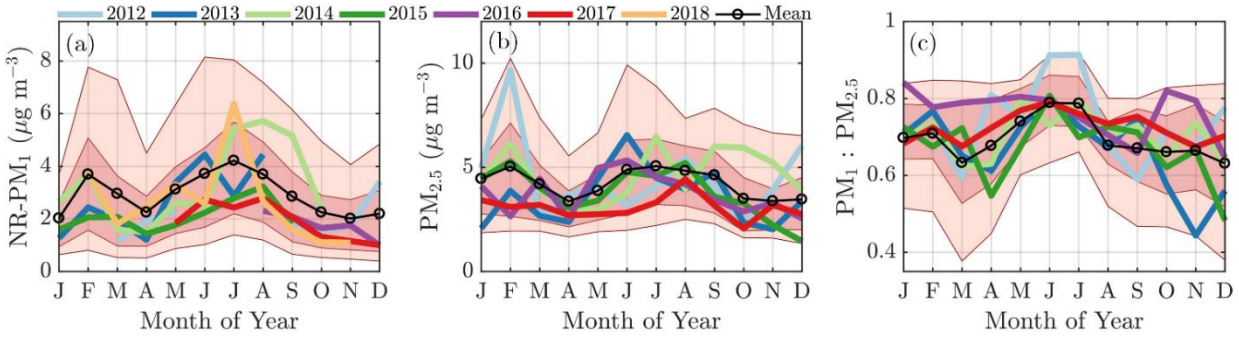

460

461 **Figure 3** The monthly cycles of NR–PM_1 (Panel a), $PM_{2.5}$ (Panel b), and the ratio between PM_1 and $PM_{2.5}$ (Panel c). The median
462 monthly values for each year are individually displayed with the coloured solid lines. The black circled line represents the overall
463 monthly mean values. The dark red shaded area is drawn between the overall 25th and 75th percentiles and the lighter red shaded area
464 between the overall 10th and 90th percentile. The x–axes represent the time of the year and the y–axes in panels a and b mass
465 concentration in µg m^{-3} and a unit less ratio in panel c.

466

467 The February PM maximum is linked to an enhanced loading of inorganic aerosol species, such as nitrate and especially
468 sulphate, as well as a slight increase of organics (Figures 4a-c), whereas the summertime maximum is explained by a
469 massive enhancement of organics alone (Figure 4a). The main precursors for inorganic aerosols, i.e. SO_2 and NO_x peak
470 during winter albeit less sharply on February alone (Figure 4e&f). As fossil fuel combustion processes are the major
471 sources of SO_2 and NO_x, their emissions likely increase during cold months due to enhanced need for residential heating,
472 for example. More importantly, these emissions are trapped in a shallow atmospheric boundary layer increasing the
473 concentration recorded within it. One possible reason for the "lack" of sulphate and nitrate aerosol outside February,
474 despite the great availability of SO_2 and NO_x, is likely related to wind direction transitioning, discussed later in the
475 manuscript. Another effect could be the darkness prohibiting photochemistry needed for inorganic aerosol formation.
476 Indeed, the global radiation measured above the forest canopy shows only a minimal short wave radiation flux in
477 November, December and early January, but it increases mid–January onwards (Figure 1b). As February is generally
478 drier (in terms of less precipitation) than the other winter months (Pirinen et al., 2012), the lifetime of aerosols could be
479 greater, making the inorganic particles more likely to reach SMEAR II. The inorganic nitrate (ammonium nitrate)
480 formation is highly dependent on ammonia availability. The ammonia concentration during wintertime is nearly
481 negligible at SMEAR II and increases rapidly in spring (Makkonen et al., 2014). The low nearby ammonia availability
482 suggests that the wintertime nitrate is long–range transport.

483

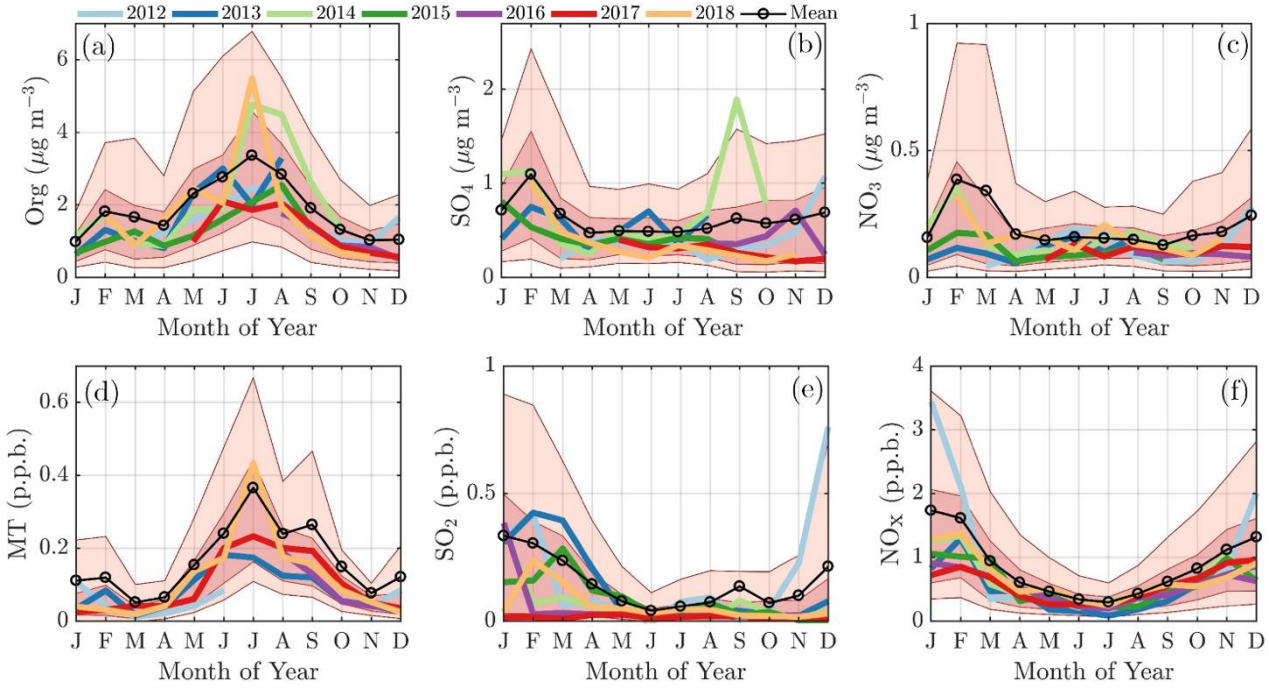

Figure 4 The monthly cycles of organics (panel a), sulphate (panel b) and nitrate (panel c) concentrations in the NR–PM_1, and their major precursors, i.e. monoterpenes (panel d), sulphur dioxide (panel e), and nitrogen oxides (panel f). The median monthly concentrations for each year are individually displayed with the coloured solid lines. The black circled line represents the overall monthly mean values. The dark red shaded area is drawn between the overall 25th and 75th percentiles and the lighter red shaded area between the overall 10th and 90th percentile. The x–axes represent the time of the year and the y–axes in panels a–c mass concentration in μg m^{-3} , and d–f in parts per billion (p.p.b.).

Monoterpenes also show a non–zero loading during all winter months (Figure 4d). Their source is likely anthropogenic, such as the nearby sawmills, rather than biogenic due to the low ambient temperature limiting their biogenic emissions (Guenther et al., 1993;Hakola et al., 2012;Kontkanen et al., 2016). Their wintertime presence could be linked to their overall decreased photochemical sink and them being emitted to the shallower atmospheric boundary layer with little vertical dilution. The monoterpene mixing ratio starts increasing rapidly in April achieving its maximum monthly median value during July (Figure 4d), simultaneously with NR–PM_1 organics (Figure 4a). Previous studies have shown that monoterpene emissions increase exponentially with ambient temperature (Guenther et al., 1993;Aalto et al., 2015). As the current study does not incorporate monoterpene emission data, we visualise the behaviour of monoterpene mixing ratio with increasing ambient temperature in Figure 5b. The increase in monoterpene mixing ratio is likely a combined result from increased biological plant activity in the forest as well as the increased emissions due to higher temperature. Organic aerosol concentration behaves in a similar manner as a function of temperature, as depicted in Figure 5a. Such behaviour in organic aerosol loading is often attributed to biogenic SOA formation from BVOCs (Daellenbach et al., 2017;Stefenelli et al., 2019;Vlachou et al., 2018;Paasonen et al., 2013).

Besides biogenic SOA, also open fire biomass burning organic aerosol (BBOA) is a major contributor to summertime organics worldwide, from wild fires during dry conditions (Bond et al., 2004;De Gouw and Jimenez, 2009;Mikhailov et al., 2017;Corrigan et al., 2013). An enhancement in eBC concentration, a tracer for BBOA, was observed as a function of temperature at SMEAR II implying the possible presence of BBOA in the summertime sub–micron aerosol (Figure

5d). However, uncertainties can be attributed to the eBC concentration as scattering coatings, such as salts or even photochemically aged SOA can also generate a lensing effect leading to an overestimation of eBC (Bond and Bergstrom, 2006;Zhang et al., 2018). Such effect could lead to a substantial overestimation of eBC especially in summertime, when the organic loading is highest. Some certainty of the BBOA and BC enhancement with high temperatures can however be retrieved from Figure 5c, where carbon monoxide (CO) mixing ratio also increases at relatively high ambient temperatures (T > 15 °C). CO is known to be emitted from incomplete combustion processes. Nonetheless, as the increase in eBC visualised in Figure 5d is less drastic than for monoterpenes, we suggest the biogenic SOA production as the major organic aerosol source in summertime. While the quantification and separation of BBOA from SOA will be the topic of an upcoming independent publication centred on the analysis of organic aerosol mass spectral fingerprints at SMEAR II, we briefly introduce the behaviour of f_{60}. $f_{60,}$ which equals the contribution of m/Q 60 Th signal to the total organic signal recorded by the ACSM, is a marker for levoglucosan-like species originating from cellulose pyrolysis in biomass burning (Schneider et al., 2006;Alfarra et al., 2007). f_{60} is present at high percentages in fresh BBOA plumes (Cubison et al., 2011), but decays due to BBOA photochemical aging into oxidised organic aerosol. The fairly rapid (in order of several hours to days) photochemical aging of BBOA has been a topic of earlier chamber (Grieshop et al., 2009;Jimenez et al., 2009) and ambient studies (DeCarlo et al., 2010;Cubison et al., 2011). Here, unlike CO and eBC, f_{60} does not increase as a function of temperature in the highest temperature bins, but stays rather constant albeit lower than the f_{60} values recorded under cold temperatures at SMEAR II (Figure 5e). As the possible wild fires contributing to SMEAR II CO and eBC under high ambient temperatures also occur further away, it is likely that the BBOA is oxidised before detected at SMEAR II. CO and eBC can be considered as more inert BBOA markers compared to f_{60}. The wintertime f_{60} is likely linked to wintertime biomass burning (for domestic heating purposes) emissions trapped in the shallow mixing layer. These emissions are discussed more later on in the manuscript (see chapter 3.2 Diurnal variation of NR–PM_1 composition)."

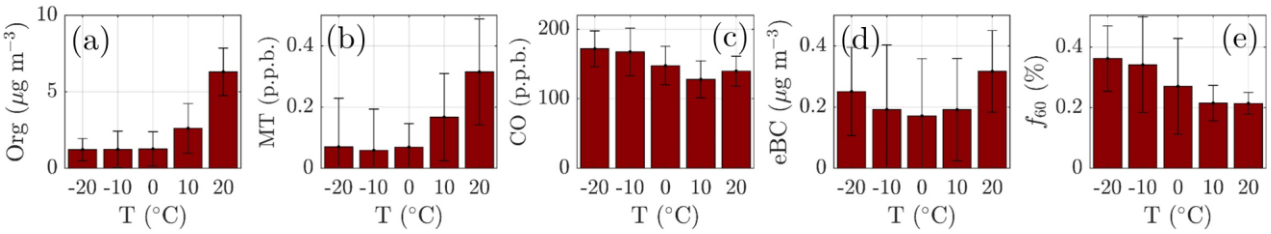

Figure 5 The daily mean organic aerosol (Org, panel a), monoterpene (MT, panel b), carbon monoxide (CO, panel c), equivalent black carbon (eBC, panel d) concentrations, and the fraction of the ACSM Org-signal made up by levoglucosan-like species (f_{60}, panel e) recorded under different ambient temperatures. The values recorded assigned into 10 °C wide bins based on the daily ambient temperature mean. The marker error bars show the standard deviation of the values in each bin.

3.1.1 Case study: The effect of warm summers on organic aerosol loading

The highest NR–PM_1 mass concentrations were detected during summers of 2014 and 2018. These summers were the hottest during the whole measurement period (Figure 6a), and linked to persistent high pressure conditions (Sinclair et al., 2019;FMI, 2014) . The non–parametric probability densities (Kernel distributions) for temperature for Julys 2012–2018, displayed individually in Figure 4a, show clearly higher temperatures in July 2014 and 2018. Indeed, these months were abnormally warm as July 2014 was 2.2°C, and July 2018 was 3.4°C higher than the 7–year July mean (16.6 °C). Comparing to the 30–year July climate at SMEAR II (1981–2010) (Pirinen et al., 2012), the mean temperature in July

2014 was 2.8°C, and July 2018 4.0°C higher. As can be seen from Figures 4a&d, both organic aerosol and monoterpene concentration positively responded to this temperature change with high median values. The same phenomenon is visualised in Figures 4b&c through Kernel densities for particulate organics and monoterpenes, respectively, for July of each year. The recorded organic aerosol concentration was 50% higher than the 7–year mean in July 2014, and 70% higher in 2018. The monoterpene concentration in turn was 50% higher in 2018 compared to the mean of all available July data (due to PTR–MS sensitivity issues, the 2014 data was chosen to be excluded from the analysis).

As the high–pressure weather ruling in Julys 2014 and 2018 further promoted clear–sky conditions, also the oxidation capacity of the air was likely affected. This could have led to efficient monoterpene oxidation towards condensable low–volatility products. Furthermore, their condensation onto particles could explain the observed high organic aerosol mass concentration. The SOA formation enhancement as a function of temperature has also been investigated previously in a modelling study, where a significant global increase in monoterpene–derived organic aerosol concentration was projected to future, following different climate scenarios introduced by the Intergovernmental Panel of Climate Change (IPCC) (Heald et al., 2008). Kourtchev et al. (2016) investigated the effect of high ambient temperature on biogenic SOA loading and composition utilising measurement data from SMEAR II. They include summers 2011 and 2014 to their analysis, where 2011 summer represents a significantly colder summer (average ambient temperature was 8°C less than in 2014). By utilising ultra–high resolution off–line mass spectrometry on filter samples collected at SMEAR II, they detected a significantly higher SOA oligomer content during 2014. Their results not only highlight the large increase in SOA mass as a function of temperature, but also on the SOA composition differences affected by the large SOA content which further influenced the CCN formation potential of SOA.

A quick revisit to the OCEC vs ACSM comparison performed earlier in the manuscript (Figure 2e) shows relatively high Org/OC-values (k = 1.68) for July 2018, which further indicates of high oxygenation of OA (Aiken et al., 2008). However, the time series of the ruling monthly Org/OC-values, visualised in Figure A.5, reveal an even higher Org/OC for August 2018. Further analysis of Org/OC recorded from SMEAR II is needed to answer whether such behaviour is frequently occurring at SMEAR II, or whether July 2018 organic aerosol was less functionalised (oxidised) than usual due to higher presence of primary organic aerosol, such as BBOA, than usual. Thus, not to link the organic aerosol increase to biogenic SOA formation exclusively, we also investigated the presence of BBOA in the sub–micron aerosol during Julys 2014 and 2018 via Kernel distributions for eBC and f_{60}, presented in Figure 6d&e. The eBC distribution clearly hints towards BBOA presence during July 2018, whereas July 2014 seems much less affected. Importantly, we also want to inform that in July 2018 we had only one week of eBC data available. The July 2018 eBC could be linked to the severe wild fires occurring in Sweden during July and August 2018. The July eBC measurement period overlaps with the forest fire occurrence period. Sweden also suffered from wild fires in August 2014, not depicted in Figure 6 that focuses on Julys alone. The f_{60} in turn follows the conclusions made earlier in the context of Figure 5 as the f_{60} values remain low each July, and approach the f_{60} background levels of 0.3% (Cubison et al., 2011; Figure 6e). Importantly, such negligible f_{60} signals were detected under the influence of an aged BBOA plume originating from Moscow and Northern Ukraine wild fires at SMEAR II also in 2010 (Corrigan et al., 2013). An AMS, which was used as one of the measurement tools in the campaign, detected mass spectra resembling oxidised organic aerosol during the biomass burning influence. These data correlated well with multiple biomass burning markers including CO, potassium and acetonitrile despite the lack of resemblance with fresh BBOA mass spectra with high f_{60}. Corrigan et al. (2013) finally attributed up to 25% of the organic

aerosol to BBOA originating from the Moscow and Northern Ukraine wild fires. 35% of the organic aerosol mass was associated with biogenic SOA formation. The weather during the Corrigan et al. (2013) study period in 2010 was also unusually warm (T_{avg} = 20°C), and resembled summers 2014 and 2018 regarding the ruling anti-cyclonic circulation pattern.

The frequency, duration and intensity of heatwaves are projected to increase in the future Finnish climate due to positive pressure anomalies over Finland and to the east of Finland, as well as a negative pressure anomaly over Russia between 90 and 120°E (Kim et al., 2018). Moreover, the IPCC states that droughts and insect outbreaks, are projected to be boosted in the warming climate (Barros et al., 2014). Recent findings by Zhao et al. (2017) show how such biotic and abiotic stress factors enhance VOC emissions from plants that further contribute to organic aerosol after oxidation (Zhao et al., 2017). Wildfires in turn are likewise likely to occur globally more frequently in the future due to increasing number of long–lasting heatwaves (Spracklen et al., 2009). Indeed, BBOA loadings due to wildfires already show a slight increase in the United States (Ridley et al., 2018). Based on these previous studies, as well as our observations together with the Corrigan et al. (2013) study from SMEAR II, the increasing frequency of heat waves and wildfires will enhance the particulate matter loading at SMEAR II in the future, and continuous long–term measurements, like the ones presented here, will be important in monitoring such changes.

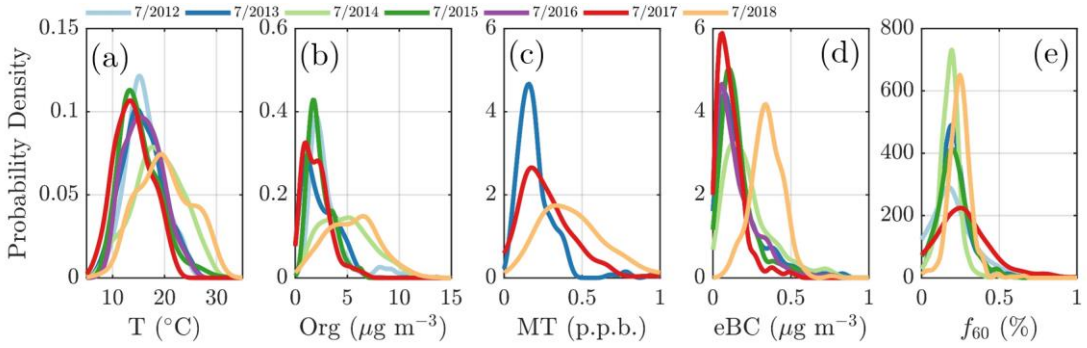

Figure 6 Non–parametric probability densities (Kernel distributions) of temperature (panel a), organic aerosol (panel b), monoterpenes (panel c), equivalent black carbon (panel d) concentrations, and the fraction of the ACSM organic signal made up by levoglucosan-like species (f_{60}; panel e) during individual Julys across the measurement period (2012–2018). The data availability for eBC was one week in July 2018. The x–axes represent the T, Org, MT and eBC values recorded, respectively and the y–axes the non–parametric probability densities. Briefly, the Kernel distributions are similar to smoothed histograms of the measurement data. This visualisation was chosen to avoid assumptions of the nature of distribution that might hide important features of the measurement data if presented with normal distributions, for instance.

3.1.2 Case study: Sulphate transport from Holuhraun flood lava eruption

The sulphate loading in September 2014 represents the largest outlier in Figure 4b with the average mass concentration five times greater than the overall September mean. The mean SO_2 concentration during September 2014 was 0.66 p.p.b., which is 0.50 p.p.b. higher than the mean SO_2 mixing ratio representing all the Septembers during the measurement period (0.16 p.p.b.). The elevated median SO_2 concentration during September 2014 is also visible in Figure 4e. To investigate the source of sulphur, we displayed the full atmospheric column SO_2 concentration during September 2014 utilising satellite observations (Figure A.6a). The SO_2 concentration hot spot was located in Iceland and is linked to the fissure Bárðarbunga–Veiðivötn eruption at Holuhraun (Aug 31st 2014 – Feb 28th 2015) that yielded 20–120 kilotons a day of SO_2 (Schmidt et al., 2015). The concentration above SMEAR II was obviously not comparable to the loading near the eruption

site. However, based on a rough trajectory analysis (Figure A.6b) we link our observations of elevated sulphate and SO_2 during September 2014 to the diluted plume from Holuhraun.

3.2 Diurnal variation of NR–PM_1 composition

The year–to–year variation in the NR–PM_1 monthly median seasonal cycles shows rather consistent behaviour throughout the measurement period and even the overall 10^{th} percentile of the PM–data suits the bimodal trend discussed in the section above. The 10^{th} percentile also agrees with the seasonal trends associated with individual NR–PM_1 chemical species, i.e. organics, sulphate and nitrate as well as their precursors (Figure 4). Few outliers observed are discussed in the chapters above (see chapters 3.1.1 Case study: The effect of warm summers on organic aerosol loading and chapter 3.1.2 Sulphate transport from Holuhraun flood lava eruption). As the year–to–year variability between different years is rather minimal, we decided to investigate the overall median temporal behaviour of aerosol chemical composition further via Figure 7. The subplots in this figure are based on data matrices of median diurnal cycles (1h resolution) for every two weeks of a year (24 × 26 matrix). The matrices are visualised with contour plots (*contourf*, MATLAB 2017a) except for Figure 7h, due to the high noise level of the time trace.

Neither the NR–PM_1 concentration nor its chemical species have large diurnal variability during wintertime (Figure 7a) due to low solar radiation and the lack of diurnal variability in ambient temperature (Figures 1a&b) prolonging the life time of aerosols. Thus, the wintertime chemical composition of NR–PM_1 stays stable over the course of the day (Figures 7b&d). As wintertime PM is presumably mostly long–range transport, its components' diurnal patterns are less obvious due their cumulative build–up in the atmosphere. For example, as sulphate aerosols, the most prominent inorganic species, are long lived due to their low volatility, we do not expect sulphate to have diurnal variation in wintertime because of the lack of major SO_2 sources at SMEAR II's proximity. The ammonium mass concentration lacks diurnal pattern as well and peaks at the same time of the year as sulphate. The degree of aerosol neutralisation by ammonia can be estimated by the ratio between the measured ammonium and the amount of ammonium needed to neutralise the anions detected by the ACSM (termed "NH_4 predicted") (Zhang et al., 2007b). The overall ratio was 0.66 hinting towards moderately acidic ammonium sulphate aerosols (Figure A.7&Figure 7h), though the uncertainty in this value is high due to the low loadings of ammonium at SMEAR II. We also acknowledge that the ratio between measured and predicted ammonium concentration is not fully accurate for acidity estimations, and if such are needed, a better estimation could be provided with thermodynamic models. The temporal variation of the ammonium balance does not show diurnal variability either, but a very modest decrease during January (Figure 7h), when the ambient temperature was the lowest. In the case of wintertime organic aerosol, the lack of a diurnal trend (Figure 7c) indicates that nearby residential heating (expected mainly in evenings) emissions are not a dominating source of organics at the site despite their clear presence in the wintertime aerosol as depicted by the seasonal f_{60} trend depicted in Figure A.4. In general, the lack of a distinct diurnal pattern rather hints towards long–range transported organics. Such conclusions can also be made based on the rather high Org/OC linear regression slope for February data (k = 1.65) depicted in Figure 2e (see also Figure A.5). As mentioned earlier, a high Org/OC-ratio indicates a higher degree of functionalisation/oxidation of organic aerosol (Aiken et al., 2008).

From March onwards, when the solar radiation flux has significantly increased, the aerosol chemical composition starts to show modest diurnal variability. The ratio between organic and inorganic aerosol chemical species (OIR) exhibits

diurnal variability from March to October, when also ambient temperature has strong diurnal variation. The OIR achieves its minimum during daytime and maximum during night (Figure 7b). In other words, particles have the highest organic fraction during night-time and early mornings. The organic aerosol mass concentration increases during night (Figure 7c), likely due to more efficient partitioning of semi–volatile species into the aerosol phase. This effect is seen even more clearly in the nitrate concentration (Figure 7e), with a strong diurnal pattern largely tracking the diurnal temperature trends over the year.

The nature of particulate nitrate can be estimated via fragmentation ratios of NO^+ and NO_2^+ ions detected by the ACSM as described by (Farmer et al., 2010) for the AMS. A higher ratio (> 5) generally means a greater presence of organic nitrates and a lower ratio (2–3) indicates inorganic ammonium nitrate. As the ACSM has a low mass resolving power, we here estimate the ratio between *m/Q* 30 and *m/Q* 46 Th as a proxy for the NO^+ : NO_2^+ –ratio. We note that there is possible interference of organic mass fragments at these *m/Q*–ratios. Nonetheless, we observe that the wintertime nitrate resembles ammonium nitrate and the summertime nitrate hints towards the presence of organic nitrates (Figure 7g). This is in line with the recent study stating that more than 50% of the nitrates detected in the sub–micron particles at SMEAR II are estimated to contain organic nitrate functionalities (Äijälä et al., 2019). However, we should stress the fact that the data coverage of wintertime was limited in the Äijälä et al. (2019) study that could lead to an overestimation of annual organic nitrate mass fraction. Such high organic nitrate fraction could also explain some of the scatter observed in the ACSM NO_3 and MARGA NO_3 comparison discussed earlier in the manuscript (Figure A.3 and chapter 2.5 ACSM chemical speciation validation). We observe no clear diurnal pattern in the fragmentation ratio.

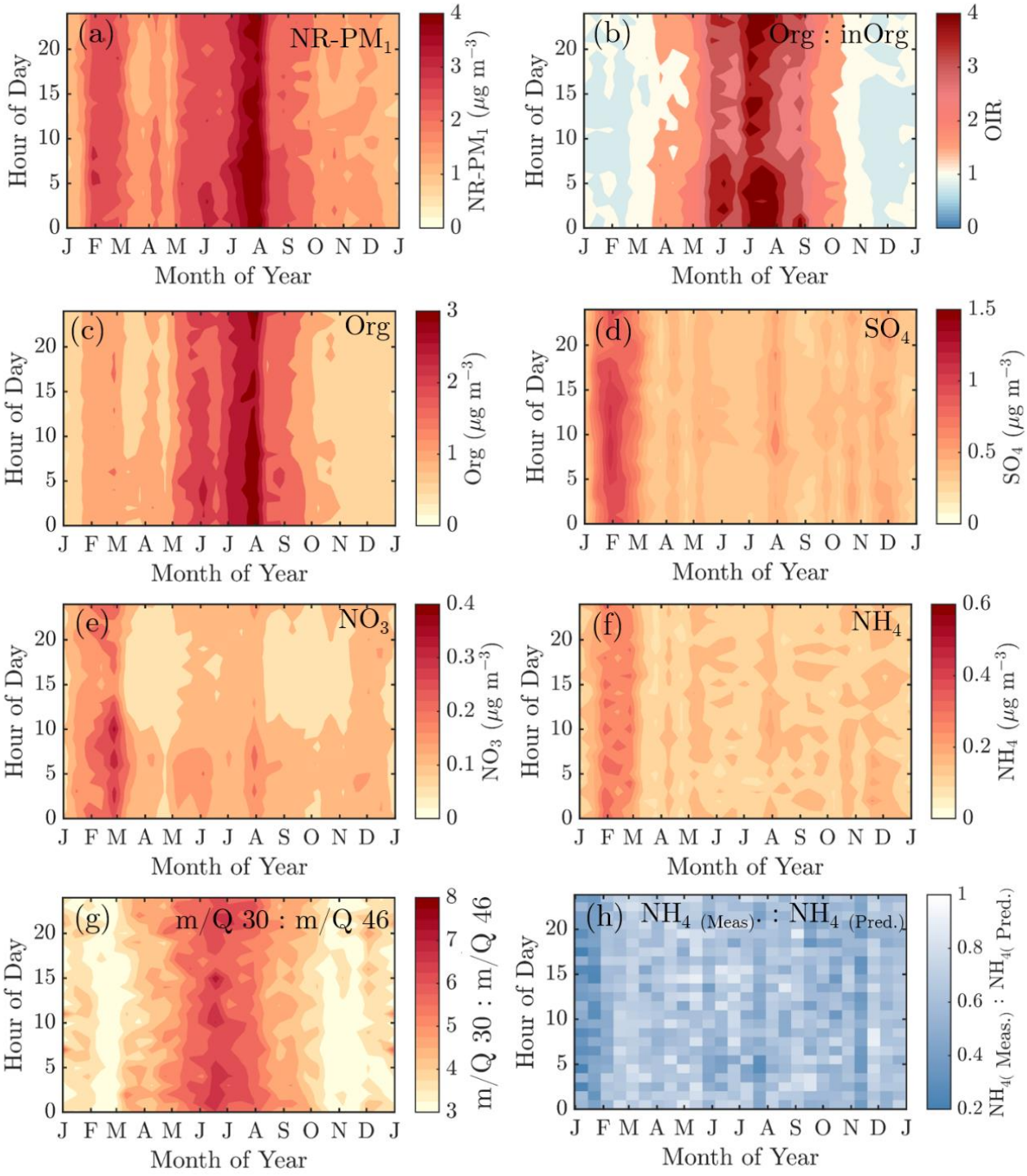

Figure 7 The median diurnal cycles of NR–PM_1 (panel a), Organic–to–inorganic ratio (panel b), organic aerosol (panel c), sulphate (panel d), nitrate (panel e), ammonium (panel f), *m/Q* 30 : *m/Q* 46 Th fragmentation ratio (panel g), and the ratio between measured and predicted ammonium (panel h). The y–axes represent the local time of day (UTC+2) and x–axes the month. The color scales present the mass concentration (panels a, c–f) or ratios (panels b, g–h). Note that the scaling of the color bar is different in all of the figures. Panels a-g include interpolation of the 14 d × 1 h resolution data grid based on the MATLAB 2017a *contourf* function. Panel h has no interpolation involved due to the high noise level of the variable. The plot is produced with MATLAB 2017a *pcolor* function.

3.3 Wind direction dependence

The wind direction plays a key role together with other meteorological conditions determining the aerosol chemical composition at SMEAR II. While the sections above focus more on the role of radiation and temperature on sub–micron aerosol composition, this section explains the role of wind direction and speed. We want to stress that this section does not include any definite geographical source analysis of the NR–PM_1 components. A detailed trajectory analysis is a better tool for understanding the actual footprint areas of air pollutants as wind direction analysis might lead to a systematic bias in the pollutant origins due to prevailing weather patterns.

3.3.1 Wind sector dependent diurnal cycles of organics and sulphate

To explore the wind direction dependence of the seasonal cycles of the main NR–PM_1 chemical species, organics and sulphate, we visualised their monthly median diurnal cycles with 4–hour time resolution (12 × 6 matrix) for four different wind direction bins: 0–90° (I), 90–180° (II), 180–270° (III), and 270–360° (IV) in Figure 8. The frequency of different wind directions are depicted in Figure A.1, showing that e.g. sector I was the least likely, while wind from sector III was the dominant direction.

The highest organic aerosol loading was observed during summer for all of the wind direction bins (I – IV) with rather modest diurnal variability, perhaps due to the coarse time resolution used (Figure 8, left panels). The greatest organic aerosol concentration was associated with sector II that covers the direction of the Korkeakoski sawmills located 6 – 7 km to the SW (Figure 8c). Moreover, the February peak in organic aerosol was also most distinguishable from sector II (Figure 8c). Sulphate aerosol in turn was mostly detected with winds from sector I and II (Figure 8, right panels). Sector I shows a general wintertime enhancement (Figure 8b), whereas sector II shows a clear maximum during February (Figure 8d). The westerly sectors (III&IV) were associated with cleaner air (Figures 8e–h).

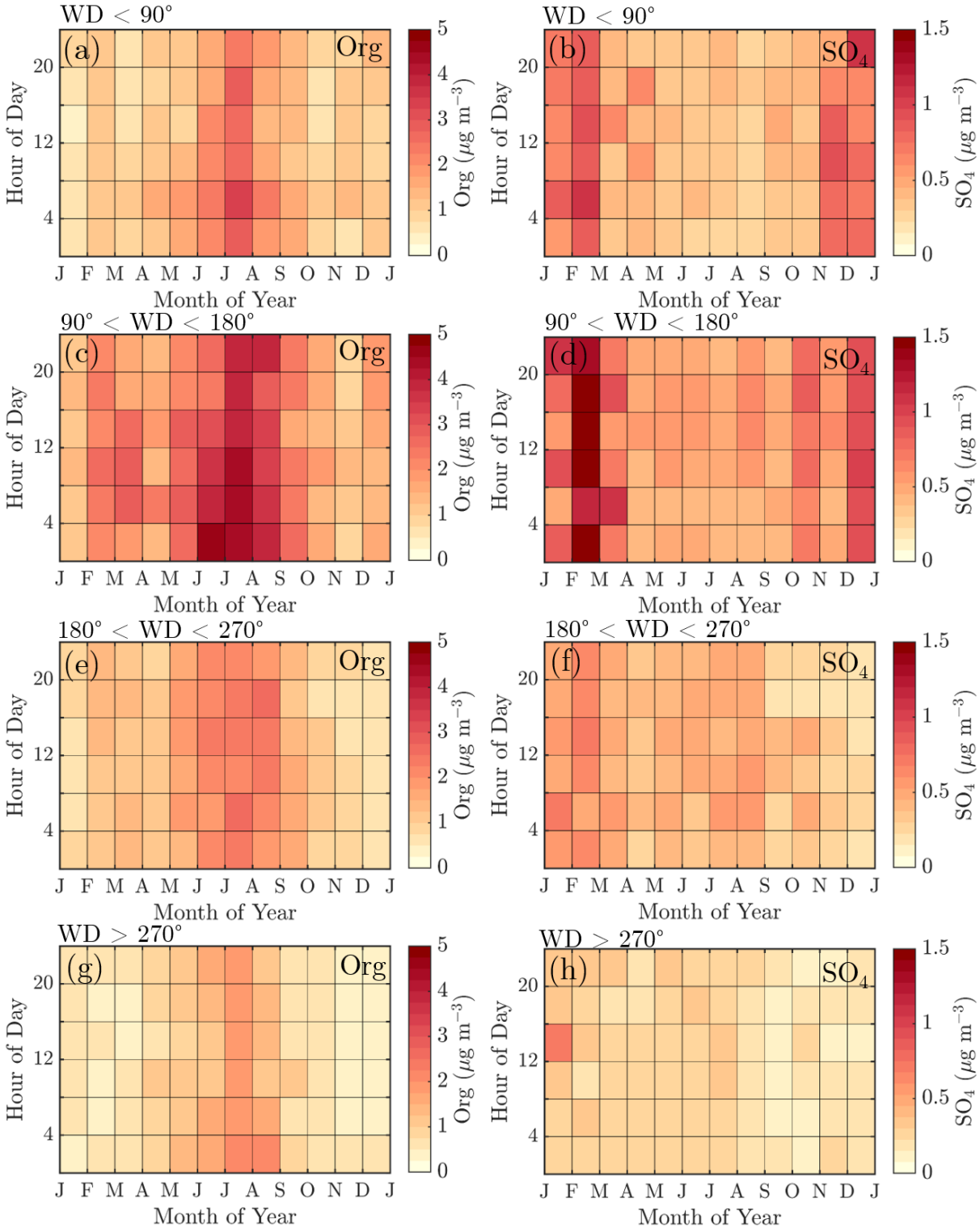

711

712 **Figure 8** Diurnal cycles of organic aerosol and sulphate divided into different wind direction bins: Panels a–b: wind direction <90°,
713 panels c–d: wind direction 90–180°, panels e–f: wind direction 180–270°, and panels g–h: wind direction >270°. The y–axes represent
714 the local time of day (UTC+2), and the x–axes the time of the year. The color scales represent the organic aerosol and sulphate aerosol
715 mass concentrations in μg m^{-3}. Figure A.1 introduces the likelihoods of each wind direction bin via a traditional wind rose plot.

716

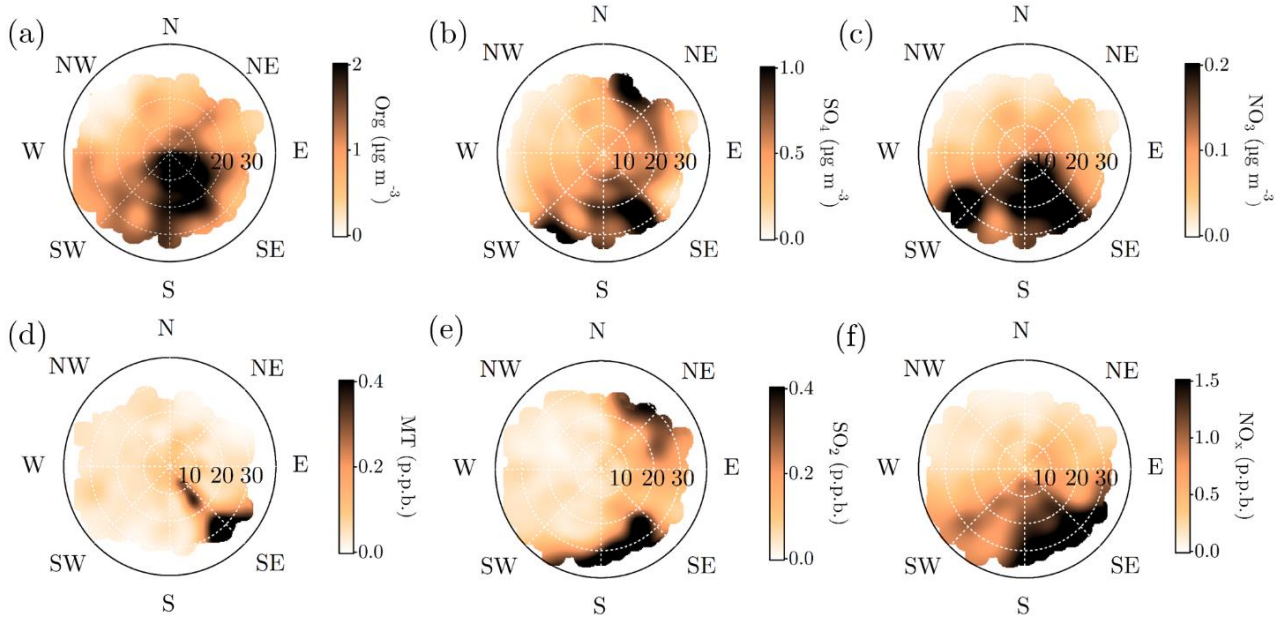

Figure 9 Openair polar plots for organic aerosol (panel a), sulphate (panel b), nitrate (panel c), monoterpenes (panel d), SO_2 (panel e), and NO_x (panel f). The distances from the origin indicates wind speeds in km h^{-1}. The wind speed grid lines are presented with white dashed circles. The colour scales represent the concentrations observed with each wind speed and direction combinations. As the figures do not indicate any likelihood of the wind speed and distance combinations, Figure A.1 is important to keep in mind while interpreting them. Briefly, N–NE–E is the least probable wind direction, whereas S–SW–W is the most likely. Wind speeds generally stay below 20 km h^{-1}.

3.3.2 Openair: Organics and monoterpenes

Finally, we investigate the aerosol chemical composition dependence of wind speed and direction utilizing openair polar plots. As the polar plots do not take into account the frequency of certain wind direction and speed combinations, Figures 1c&d and Figure A.1 are important when drawing conclusions based on them.

Organic aerosol concentration at SMEAR II increased with S–SE winds as already visualised also in Figure 8c (Figure 9a). The monoterpene mixing ratio also peaked, with a more narrow range of wind directions, analogous with the direction of the nearby Korkeakoski sawmills (Figure 9d). With higher wind speeds, monoterpenes were also observed from a wider span of wind directions. Organic aerosol showed wind speed dependence with S–SE winds with lower concentrations associated with wind speed exceeding 25 km h^{-1} (ca. 6.9 m s^{-1}). A possible explanation is that the monoterpene emissions from the sawmills did not have time to oxidise and form SOA with such high wind speeds before reaching SMEAR II. Organic aerosol concentration was relatively constant outside the sawmill interference, though the lowest loadings were detected when air masses arrived with wind speeds exceeding 20 km h^{-1} (ca. 5.5 m s^{-1}) from the NW sector. In contrast, monoterpene mixing ratio was rather constant with varying wind directions and wind speeds, obviously again apart from the sawmills direction (approximately 130°). Similar observations of the wind direction dependence of monoterpene mixing ratios have been reported before, with a subsequent organic aerosol mass concentration increase at SMEAR II with SW winds (Eerdekens et al., 2009;Liao et al., 2011).

A simplified seasonal analysis on aerosol chemical composition wind dependence was performed by investigating the openair polar plots for all data recorded in February (**Figure A.1**Figure A.8) and July (Figure A.9). Korkeakoski sawmills represented the main monoterpene source in February as the concentration coinciding with air masses arriving from other directions was negligible (Figure A.8d). In February, the sawmill emissions did not significantly enhance the organic aerosol concentration at the site, due to low oxidation rates (monoterpene life time up to 10 h; Peräkylä et al., 2014) and higher wind speeds (Figure A.8a). The organic aerosol concentration approached zero with NW winds during February regardless of the wind speed. A major wind speed influence can be observed with SW winds, as higher wind speeds coincide with elevated organic loading.

In July, the monoterpene mixing ratio increased regardless of the wind direction due to increased biogenic emissions from the surrounding forest, but also the sawmill influence remained elevated (Figure A.9d). The monoterpene life time in July is roughly two hours (Peräkylä et al., 2014) indicating an efficient photochemical sink. Thus, monoterpene sources are likely not that far. The organic aerosol concentration was clearly overall elevated, however the overall easterly interference was more pronounced compared to February (Figures A.9a). It could be linked to the high pressure systems often associated with easterly winds that bring warm air and clear sky conditions to SMEAR II promoting BVOC emissions and SOA formation as discussed earlier in the paper.

3.3.3 Openair: Sulphate and SO_2

Relatively high concentrations of sulphate aerosols and sulphur dioxide were detected with N–NE and SE–SW winds (Figures 9b&e). Riuttanen et al. (2013) performed a HYSPLIT trajectory analysis for SMEAR II for 1996–2008 with SO_2 concentration fields showing similar results. They attribute the detected SO_2 to anthropogenic emission sources in St. Petersburg, Baltic region, Kola Peninsula and the SE corner of the White Sea. In addition to the major emission sources introduced by Riuttanen et al. (2013), also paper and pulp industry are major known SO_2 emitters. Several paper and pulp mills are situated in Finland, mostly NE and SE from SMEAR II (Metsäteollisuus, 2018). Another national major SO_2 source is certainly the Kilpilahti (Porvoo) oil refinery, located ~200 km S-SE from SMEAR II. This area represents the most extensive oil refinery and chemical industry in the Nordic countries, and the SO_2 concentrations measured downwind from the area have been close to those obtained from Kola Peninsula outflow (Sarnela et al., 2015).

Large emission sources located SW of SMEAR II listed by EMEP (European Monitoring and Evaluation Programme) did not stand out in the analysis performed by Riuttanen et al. (2013), but a wind direction dependence visible in the current study, associated only with high wind speeds. Similar wind speed dependence was observed with SE–S and N–NE winds as the concentration of sulphate and SO_2 clearly increased when wind speeds exceeded 20 km h^{-1} (ca. 5.5 m s^{-1}). Such wind speed dependence can be observed with long–range transported air pollutants: their transport is generally more efficient with higher wind speeds. The results presented here are also consistent with hygroscopicity measurements conducted at SMEAR II (Petäjä et al., 2005), where the hygroscopic growth factor was greatest when SO_2 rich air arrived fast to the station from the NE.

NE and SE represent the major SO_2 sources in February. The NE SO_2 was detected with lower wind speed dependence than generally observed (Figures A.8b&e). The lifetime of SO_2 is dependent on wet and dry deposition, and oxidation to sulphate (photochemistry or aqueous phase chemistry in cloud droplets). These factors influence the likelihood of

detecting SO_2 from distant sources. The higher wintertime concentrations are also linked to the atmospheric boundary layer dynamics, as discussed earlier. The SW and SE–S winds with wind speeds exceeding 16 km h^{-1} (ca. 4.4 m s^{-1}) were associated with sulphate during February (Figure A.8b). Sulphate was detected also with a wide range of wind directions during low wind speeds. In the case of low wind speeds, it is hard to determine the wind direction accurately. However, it was clear that sulphate was not associated with W–NW winds, as shown previously in the paper (Figure 8, right panels).

The sulphate openair polar plots for July (Figure A.9b) reveals that the sulphate transport was more wind speed dependent than in February. Moreover, the wind directions linked to sulphate presence at SMEAR II were NW–N, NE, and E–SE, but observed only when the wind speeds exceeded 16 km h^{-1} (ca. 4.4 m s^{-1}). SO_2 was only observed with wind speeds exceeded 16 km h^{-1} (ca. 4.4 m s^{-1}) with NE winds (Figure A.9e). High wind speeds are needed in July to transport rather short–lived pollutants, such as SO_2, to SMEAR II from distant sources.

As can be seen from Figures 9e, A.8e & A.9e, elevated SO_2 concentrations (dark areas in the concentration fields) are associated with very specific, rather narrow ranges of easterly (mainly NE and SE) wind directions, and elevated wind speeds (> 16 – 20 km h^{-1}). These figures illustrate the sensitivity of the recorded SO_2 concentration towards even moderate wind direction and speed variations. As wind direction and speed can vary significantly in an inter-annual scale, also inter-annual variability in SO_2 concentration can be expected. This could finally explain the SO_2 inter-annual variability highlighted especially in winter months (Figure 4e). Such strong variability is not reflected further in the sulphate aerosol (Figure 4b) year-to-year scales due to its long lifetime and build-up in the atmosphere.

3.3.4 Openair: Nitrate and NO_x

The nitrate concentration field visualised in Figure 9c was highest when wind blew from SE– SW. No wind speed dependence could be attributed to the nitrate from E–SE, whereas for SW, nitrate concentration clearly elevated when wind speed exceeded 20 km h^{-1} (ca. 5.5 m s^{-1}). NO_x concentration, in turn, was not significantly elevated with SW winds regardless of the wind speed, but shows similar behaviour to nitrate with SE–S winds (Figure 9f). The nitrates arriving with SW likely spend more time in the atmosphere than in the case of SE–S source. A previous study focusing on organic nitrates at SMEAR II linked their occurrence to SE winds (Kortelainen et al., 2017). They suggest night–time nitrate radical oxidation of sawmill BVOCs as their major source. The same study attributes inorganic ammonium nitrate with SW winds. The study was conducted in spring–time. Also our results suggested an increased organic nitrate presence in spring compared to wintertime (Figure 7g).

In February, the nitrate concentration field resembles the overall concentration field depicted in Figure 9c, but highest loadings were typically associated with low wind speeds from S–SE (Figure A.8c). The reason for not observing nitrate with high wind speeds could be the fact that there is not enough time for nitrate aerosol formation. NO_x concentration was overall elevated between NE and SE, and the clean SE–N sector had negligible NO_x loading (Figure A.8f). Despite the NO_x availability in the North, no nitrate aerosol was observed. This could be due to limited ammonia availability in winter time. Most NO_x was detected with E–SE winds when wind speed was 8–16 km h^{-1} (ca. 2.2–4.4 m s^{-1}).

In July, SW winds blew most of the nitrate to SMEAR II (Figure A.9c). However, also slightly elevated concentrations can be observed with S–SE winds (Figure A.9c). The nitrate associated with SW winds again requires high wind speeds.

The NO_x concentration was significantly lower in July compared to February, as already shown in Figure 4f (Figure A.9f). No clear wind speed dependence was observed.

3.3.4 Openair: Ammonium and ion balance

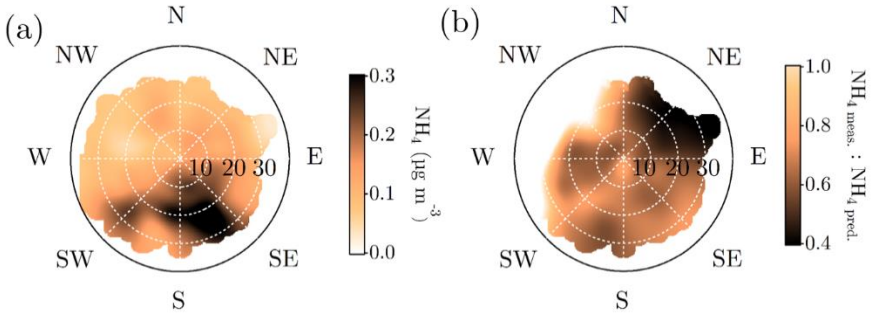

Figure 10 Openair polar plots for ammonium (panel a), and the ratio between measured and predicted ammonium (panel b). The distances from the origin indicates wind speeds in km h^{-1}. The wind speed grid lines are presented with white dashed circles. The color scales represent the concentration (panel a) and the unitless ammonium ion balance ratio (panel b) observed with each wind speed and direction combinations. As the figures do not indicate any likelihood of the wind speed and distance combinations, Figure A.1 is important to keep in mind while interpreting them. Briefly, N–NE–E is the least probable wind direction, whereas S–SW–W is the most likely. Wind speeds generally stay below 20 km h^{-1}.

The overall polar plot for ammonium, visualised in Figure 10a, did not show elevated abundance with N-NE winds in contrary to sulphate polar plot (Figure 9b). Moreover, the ammonium ion balance showed lowest values with N–NE winds that often carry the sulphate–rich aerosols to SMEAR II (Figures 9b&10b). Such observations hint towards acidic aerosols. Riva et al. (2019) observed acidic aerosols likely originating from the Kola Peninsula that support this hypothesis. Moreover, the particle acidity further drove chemical transformations in the aerosol organic leading to a higher presence of oligomers in the aerosol. Also the hygroscopicity analysis carried out at SMEAR II back in 2005 showed how the particles arriving from NE were most hygroscopic (Petäjä et al., 2005) that is a property boosted in acidic aerosols. The clean NW sector shows bright values for the ammonium balance field. Here, the ammonium balance exceeds one due to the noisiness of the data introduced by both ammonium and nitrate used in the ammonium balance calculation being below their detection limits during NW winds.

4 Conclusions

To better understand the boreal forest aerosol, an aerosol chemical speciation monitor (ACSM) was installed for long–term monitoring of sub-micron aerosol chemical composition in 2012 at research site of SMEAR II. The measurements continue to this day. Such measurements at the site had been previously conducted only in short–term intensive measurement campaigns, leaving our understanding of the seasonal and year–to–year variability lacking. The current study spans over the first seven years (2012–2018) of on–line monitoring of the sub–micron non–refractory aerosol composition, finally providing this missing piece in SMEAR II aerosol documentation.

The median mass concentration over the measurement period was 2.3 µg m^{-3} (1.2 and 4.0 µg m^{-3} for the 25th and 75th percentiles, respectively) of which 68% was organics, 20% sulphate, 6% nitrate, and 6% ammonium. Chloride concentrations in the non–refractory sub–micron particles were negligible (< 1%). As many factors, such as ambient

temperature, solar radiation, atmospheric boundary layer height and wind influence the aerosol particle concentrations and trace gas emissions, oxidation and volatility, we observed a clear seasonal cycle in NR-PM_1 loading and composition.

During warm months, biogenic VOC emissions increase, and upon oxidation, produce SOA which represents a major source of PM at SMEAR II. Organic aerosol mass concentration achieved its annual maximum in July (3.3, 1.7, and 4.6 μg m^{-3} for median, 25^{th} and 75^{th} percentiles, respectively) that further lead to the annual maximum in the total NR-PM_1 loading (4.2, 2.2, and 5.7 μg m^{-3} for median, 25^{th}, 75^{th} percentiles, respectively). Organics on average made up 80% of the NR-PM_1 in summer. During the exceptionally hot Julys of 2014 and 2018, the organic aerosol concentrations were up to 70% higher than the 7–year July mean. Most of the mass could be associated with increased biogenic SOA production. The projected increase of heat wave frequency over Finland (and in general) will most likely influence the loading and chemical composition of aerosol particles, and subsequently affect the Earth's radiative balance. Also from this perspective, continuing the long–term measurements at SMEAR II is essential.

Winter months indicate low amounts of solar radiation and a shallow boundary layer. NO_x and SO_2, the main precursors for particulate nitrate and sulphate, respectively, achieved their maximum mixing ratios during the darkest months while emitted into the shallow boundary layer during the period of low photochemical activity. These species are generally emitted in combustion processes that lead to high wintertime concentrations both due to the additional need of residential heating as well as the shallow boundary layer prohibiting their vertical mixing. The maximum wintertime NR-PM_1 concentration was most commonly detected in February, and explained by an enhancement of inorganic aerosol species. The particulate sulphate and nitrate peaked in February, which was later than their precursors, as a combined result of wind patterns, deposition mechanisms and photochemistry affecting their formation and removal rates. The contribution of inorganic aerosol species was ca. 50% of the total NR-PM_1 (2.7, 1.6, 5.1 μg m^{-3} for median, 25^{th}, 75^{th} percentiles, respectively) in February of which 30% was sulphate, 10% nitrate and 10% ammonium. Importantly, much of these inorganic aerosol species were most likely from long-range transport. If emission regulations regarding SO_2 and NO_x become stricter in the future in Europe, and especially in Russia, the wintertime NR-PM_1 might decrease significantly at SMEAR II.

To our understanding, this is the longest time series reported describing the aerosol chemical composition measured on–line in the boreal region. Long-term monitoring of changes introduced by emission regulations together with the changes introduced by the changing climate, are crucial for understanding the aerosol-sensitivity of the (boreal) climate. Thus, we keep the ACSM measurements on going at SMEAR II to obtain an even longer data set. The data presented here will be publicly available, and we welcome collaborative work in utilising this information for broadening the understanding of the boreal environment.

Data availability

The ACSM data are available at EBAS database (http://ebas.nilu.no/). The trace gas and meteorology data are available at the SMART SMEAR data repository (https://avaa.tdata.fi/web/smart). Other data are available upon request from the corresponding authors.

Author contributions

LH, MÄ, ME, TP, MK, and DW designed the study. LH, MÄ and MA performed the ACSM measurements. LH processed and analysed the ACSM data. JA and PR performed the PTR-MS measurements and data processing. HK provided and processed the Dekati impactor data. PA performed the DMPS measurements and data processing. UM provided and processed the MARGA data. KL provided and processed the Aethalometer data. DA performed satellite and trajectory analysis in Figure A.6. LH performed the overall analysis, data visualisation and wrote the paper. ME supervised the process. All authors commented and edited the paper.

Competing interests

The authors declare no conflict of interest.

Acknowledgements

First, we thank SMEAR II staff, Petri Keronen, Erkki Siivola and Frans Korhonen for measurement maintenance and support. We thank the ACMCC, COST–COLOSSAL, and Aerodyne Research for the guidance towards high–quality instrument operation. We thank Otso Peräkylä and Jenni Kontkanen for useful discussions. For financial support, we acknowledge the European Research Council Starting Grant COALA. We thank the anonymous reviewers for their expertise.

References

Aalto, J., Porcar-Castell, A., Atherton, J., Kolari, P., Pohja, T., Hari, P., Nikinmaa, E., Petäjä, T., and Bäck, J.: Onset of photosynthesis in spring speeds up monoterpene synthesis and leads to emission bursts, Plant, cell and environment, 38, 2299-2312, 2015.

Aalto, P., Hämeri, K., Becker, E., Weber, R., Salm, J., Mäkelä, J. M., Hoell, C., O'dowd, C. D., Hansson, H.-C., Väkevä, M., Koponen, I., Gintautas, B., and Kulmala, M.: Physical characterization of aerosol particles during nucleation events, Tellus B: Chemical Physical Meteorology, 53, 344-358, 2001.

Aas, W., Mortier, A., Bowersox, V., Cherian, R., Faluvegi, G., Fagerli, H., Hand, J., Klimont, Z., Galy-Lacaux, C., Lehmann, C. M., Lund Myhre, C., Myhre, G., Olivié, D., Sato, K., Quaas, J., Rao, P. S. P., Schultz, M., Shindell, D., Skeie, R. B., Stein, A., Takemura, T., Tsyro, S., Vet, R., and Xu, X.: Global and regional trends of atmospheric sulfur, Scientific reports, 9, 953, 2019.

Aiken, A. C., Decarlo, P. F., Kroll, J. H., Worsnop, D. R., Huffman, J. A., Docherty, K. S., Ulbrich, I. M., Mohr, C., Kimmel, J. R., Sueper, D., Sun, Y., Zhang, Q., Trimborn, A., Northway, M., Ziemann, P. J., Canagaratna, M. R., Onasch, T. B., Alfarra, R. M., Prevot, A. S. H., Dommen, J., Duplissy, J., Metzger, A., Baltensperger, U., and Jimenez, J. L.: O/C and OM/OC ratios of primary, secondary, and ambient organic aerosols with high-resolution time-of-flight aerosol mass spectrometry, Environmental Science and Technology, 42, 4478-4485, 2008.

Alfarra, M. R., Prevot, A. S., Szidat, S., Sandradewi, J., Weimer, S., Lanz, V. A., Schreiber, D., Mohr, M., and Baltensperger, U.: Identification of the mass spectral signature of organic aerosols from wood burning emissions, Environmental Science and Technology, 41, 5770-5777, 2007.

Allan, J. D., Delia, A. E., Coe, H., Bower, K. N., Alfarra, M. R., Jimenez, J. L., Middlebrook, A. M., Drewnick, F., Onasch, T. B., Canagaratna, M. R., Jayne, J. T., and Worsnop, D. R.: A generalised method for the extraction of chemically resolved mass spectra from Aerodyne aerosol mass spectrometer data, Journal of Aerosol Science, 35, 909-922, 2004.

Allan, J. D., Alfarra, M. R., Bower, K. N., Coe, H., Jayne, J. T., Worsnop, D. R., Aalto, P. P., Kulmala, M., Hyötyläinen, T., Cavalli, F., and Laaksonen, A.: Size and composition measurements of background aerosol and new particle growth in a Finnish forest during QUEST 2 using an Aerodyne Aerosol Mass Spectrometer, Atmospheric Chemistry and Physics, 6, 315-327, 2006.

Anttila, P., and Tuovinen, J.-P.: Trends of primary and secondary pollutant concentrations in Finland in 1994–2007, Atmospheric Environment, 44, 30-41, 2010.

Barreira, F. M., Luis, Duporte, G., Parshintsev, J., Hartonen, K., Jussila, M., Aalto, J., Bäck, J., Kulmala, M., and Riekkola, M.-L.: Emissions of biogenic volatile organic compounds from the boreal forest floor and understory, Boreal Environment Research, 2017.

Barros, V., Field, C., Dokken, M., Mastrandrea, K., TE, M., M, B., KL, C., YO, E., RC, E., B, G., ES, G., ES, K., AN, L., S, M., PR, M., and White, L.: IPCC, 2014: Climaye Change 2014: Impacts, adaptation and vulnerability: Part B:

Regional aspects. Contribution of Working Group II to the Fifth Assessment Report of the Intergovernmental Panel on Climate Change, in: IPCC, 2014: Climaye Change 2014: Impacts, adaptation and vulnerability: Part B: Regional aspects. Contribution of Working Group II to the Fifth Assessment Report of the Intergovernmental Panel on Climate Change, Cambridge University Press, 688, 2014.
Bauer, J. J., Yu, X. Y., Cary, R., Laulainen, N., and Berkowitz, C.: Characterization of the Sunset Semi-Continuous Carbon Aerosol Analyzer, Journal of the Air & Waste Management Association, 59, 826-833, 10.3155/1047-3289.59.7.826, 2009.
Bond, T. C., Streets, D. G., Yarber, K. F., Nelson, S. M., Woo, J. H., and Klimont, Z.: A technology-based global inventory of black and organic carbon emissions from combustion, Journal of Geophysical Research: Atmospheres, 109, 2004.
Bond, T. C., and Bergstrom, R. W.: Light absorption by carbonaceous particles: An investigative review, Aerosol Science and Technology, 40, 27-67, 2006.
Boucher, O., Randall, D., Artaxo, P., Bretherton, C., Feingold, G., Forster, P., Kerminen, V.-M., Kondo, Y., Liao, H., and Lohmann, U.: Clouds and aerosols, in: Climate change 2013: the physical science basis. Contribution of Working Group I to the Fifth Assessment Report of the Intergovernmental Panel on Climate Change, Cambridge University Press, 571-657, 2013.
Canagaratna, M. R., Jayne, J. T., Jimenez, J. L., Allan, J. D., Alfarra, M. R., Zhang, Q., Onasch, T. B., Drewnick, F., Coe, H., Middlebrook, A., Delia, A., Williams, L. R., Trimborn, A. M., Northway, M. J., DeCarlo, P. F., Kolb, C. E., Davidovits, P., and Worsnop, D. R.: Chemical and microphysical characterization of ambient aerosols with the aerodyne aerosol mass spectrometer, Mass Spectrometry Reviews, 26, 185-222, 10.1002/mas.20115, 2007.
Carslaw, D. C., and Ropkins, K.: Openair—an R package for air quality data analysis, Environmental Modelling & Software, 27, 52-61, 2012.
Cavalli, F., Facchini, M., Decesari, S., Emblico, L., Mircea, M., Jensen, N., and Fuzzi, S.: Size-segregated aerosol chemical composition at a boreal site in southern Finland, during the QUEST project, Atmospheric Chemistry and Physics, 6, 993-1002, 2006.
Cavalli, F., Viana, M., Yttri, K. E., Genberg, J., and Putaud, J.-P.: Toward a standardised thermal-optical protocol for measuring atmospheric organic and elemental carbon: the EUSAAR protocol, Atmospheric Measurement Techniques, 3, 2010.
Collaud Coen, M., Andrews, E., Asmi, A., Baltensperger, U., Bukowiecki, N., Day, D., Fiebig, M., Fjæraa, A. M., Flentje, H., Hyvärinen, A., Jefferson, A., Jennings, S. G., Kouvarakis, G., Lihavainen, H., Lund Myhre, C., Malm, W. C., Mihapopoulos, N., Molenar, J. V., O'Dowd, C., Ogren, J. A., Schichtel, B. A., Sheridan, P., Virkkula, A., Weingartner, E., Weller, R., and Laj, P.: Aerosol decadal trends–Part 1: In-situ optical measurements at GAW and IMPROVE stations, Atmospheric Chemistry and Physics, 13, 869-894, 2013.
Corrigan, A. L., Russell, L. M., Takahama, S., Äijälä, M., Ehn, M., Junninen, H., Rinne, J., Petäjä, T., Kulmala, M., Vogel, A. L., Hoffmann, T., Ebben, C. J., Geiger, F. M., Chhabra, P., Seinfeld, J. H., Worsnop, D. R., Song, W., Auld, J., and Williams, J.: Biogenic and biomass burning organic aerosol in a boreal forest at Hyytiälä, Finland, during HUMPPA-COPEC 2010, Atmospheric Chemistry and Physics, 13, 12233-12256, 10.5194/acp-13-12233-2013, 2013.
Crippa, M., Canonaco, F., Lanz, V., Äijälä, M., Allan, J., Carbone, S., Capes, G., Ceburnis, D., Dall'Osto, M., Day, D., DeCarlo, P. F., Ehn, M., Eriksson, A., Freney, E., Hildebrandt Ruiz, L., Hillamo, R., Jimenez, J. L., Junninen, H., Kiendler-Scharr, A., Kortelainen, A.-M., Kulmala, M., Laaksonen, A., Mensah, A. A., Mohr, C., Nemitz, E., O'Dowd, C., Ovadnevaite, J., Pandis, S. N., Petäjä, T., Poulain, L., Saarikoski, S., Sellegri, K., Swietlicki, E., Tiitta, P., Worsnop, D. R., Baltensperger, U., and Prévôt, A. S. H.: Organic aerosol components derived from 25 AMS data sets across Europe using a consistent ME-2 based source apportionment approach, Atmospheric Chemistry and Physics, 14, 6159-6176, 2014.
Cubison, M., Ortega, A., Hayes, P., Farmer, D., Day, D., Lechner, M., Brune, W. H., Apel, E., Diskin, G., Fisher, J., Hecobian, A., Knapp, D., Mikoviny, T., Riemer, D., Sache, G., Sessions, W., Weber, R., Weinheimer, A., Wisthaler, A., and Jimenez, J. L.: Effects of aging on organic aerosol from open biomass burning smoke in aircraft and laboratory studies, Atmospheric Chemistry and Physics, 11, 12049-12064, 2011.
Dada, L., Paasonen, P., Nieminen, T., Buenrostro Mazon, S., Kontkanen, J., Peräkylä, O., Lehtipalo, K., Hussein, T., Petäjä, T., Kerminen, V.-M., Bäck, J., and Kulmala, M.: Long-term analysis of clear-sky new particle formation events and nonevents in Hyytiälä, Atmospheric Chemistry and Physics, 17, 6227-6241, 2017.
Daellenbach, K. R., Stefenelli, G., Bozzetti, C., Vlachou, A., Fermo, P., Gonzalez, R., Piazzalunga, A., Colombi, C., Canonaco, F., Hueglin, C., Kasper-Giebl, A., Jaffrezo, J.-L., Bianchi, F., Slowik, J. G., Baltensperger, U., El-Haddad, I., and Prévôt, A. S. H.: Long-term chemical analysis and organic aerosol source apportionment at nine sites in central Europe: source identification and uncertainty assessment, Atmospheric Chemistry and Physics, 17, 13265-13282, 2017.
De Gouw, J., and Jimenez, J. L.: Organic aerosols in the Earth's atmosphere. ACS Publications, 2009.
DeCarlo, P., Ulbrich, I., Crounse, J., Foy, B. d., Dunlea, E., Aiken, A., Knapp, D., Weinheimer, A., Campos, T., Wennberg, P. J. A. C., and Physics: Investigation of the sources and processing of organic aerosol over the Central Mexican Plateau from aircraft measurements during MILAGRO, 10, 5257-5280, 2010.

Drinovec, L., Močnik, G., Zotter, P., Prévôt, A., Ruckstuhl, C., Coz, E., Rupakheti, M., Sciare, J., Müller, T., Wiedensohler, A., and Hansen, A.: The" dual-spot" Aethalometer: an improved measurement of aerosol black carbon with real-time loading compensation, Atmospheric Measurement Techniques, 8, 1965-1979, 2015.
Eerdekens, G., Yassaa, N., Sinha, V., Aalto, P., Aufmhoff, H., Arnold, F., Fiedler, V., Kulmala, M., and Williams, J.: VOC measurements within a boreal forest during spring 2005: on the occurrence of elevated monoterpene concentrations during night time intense particle concentration events, Atmospheric Chemistry and Physics, 9, 8331-8350, 2009.
Fanourgakis, G. S., Kanakidou, M., Nenes, A., Bauer, S. E., Bergman, T., Carslaw, K. S., Grini, A., Hamilton, D. S., Johnson, J. S., Karydis, V. A., Kirkevåg, A., Kodros, J. K., Lohmann, U., Luo, G., Makkonen, R., Matsui, H., Neubauer, D., Pierce, J. R., Schmale, J., Stier, P., Tsigaridis, K., van Noije, T., Wang, H., Watson-Parris, D., Westervelt, D. M., Yang, Y., Yoshioka, M., Daskalakis, N., Decesari, S., Gysel-Beer, M., Kalivitis, N., Liu, X., Mahowald, N. M., Myriokefalitakis, S., Schrödner, R., Sfakianaki, M., Tsimpidi, A. P., Wu, M., and Yu, F.: Evaluation of global simulations of aerosol particle and cloud condensation nuclei number, with implications for cloud droplet formation, Atmospheric Chemistry and Physics, 19, 8591-8617, 2019.
Farmer, D., Matsunaga, A., Docherty, K., Surratt, J., Seinfeld, J., Ziemann, P., and Jimenez, J.: Response of an aerosol mass spectrometer to organonitrates and organosulfates and implications for atmospheric chemistry, Proceedings of the National Academy of Sciences, 107, 6670-6675, 2010.
Finessi, E., Decesari, S., Paglione, M., Giulianelli, L., Carbone, C., Gilardoni, S., Fuzzi, S., Saarikoski, S., Raatikainen, T., Hillamo, R., Allan, J. D., Mentel, T. F., Tiitta, P., Laaksonen, A., Petäjä, T., Kulmala, M., Worsnop, D., and Facchini, M.: Determination of the biogenic secondary organic aerosol fraction in the boreal forest by NMR spectroscopy, Atmospheric Chemistry and Physics, 12, 941-959, 2012.
An exceptionally long heatwave: https://en.ilmatieteenlaitos.fi/press-release-archive/-/journal_content/56/31422/10014539, access: 13 January 2020, 2014.
Gauthier, S., Bernier, P., Kuuluvainen, T., Shvidenko, A., and Schepaschenko, D.: Boreal forest health and global change, Science, 349, 819-822, 2015.
Grieshop, A., Donahue, N., and Robinson, A.: Laboratory investigation of photochemical oxidation of organic aerosol from wood fires 2: analysis of aerosol mass spectrometer data, Atmospheric Chemistry and Physics, 9, 2227-2240, 2009.
Guenther, A. B., Zimmerman, P. R., Harley, P. C., Monson, R. K., and Fall, R.: Isoprene and monoterpene emission rate variability: model evaluations and sensitivity analyses, Journal of Geophysical Research: Atmospheres, 98, 12609-12617, 1993.
Hakola, H., Hellén, H., Hemmilä, M., Rinne, J., and Kulmala, M.: In situ measurements of volatile organic compounds in a boreal forest, Atmospheric Chemistry and Physics, 12, 11665-11678, 2012.
Hari, P., and Kulmala, M.: Station for measuring ecosystem-atmosphere relations (SMEAR II), Boreal Environment Research, 10, 315-322, 2005.
Heald, C., Henze, D., Horowitz, L., Feddema, J., Lamarque, J. F., Guenther, A., Hess, P., Vitt, F., Seinfeld, J., Goldstein, A., and Fung, I.: Predicted change in global secondary organic aerosol concentrations in response to future climate, emissions, and land use change, Journal of Geophysical Research: Atmospheres, 113, 2008.
Hong, J., Häkkinen, S. A., Paramonov, M., Äijälä, M., Hakala, J., Nieminen, T., Mikkilä, J., Prisle, N. L., Kulmala, M., Riipinen, I., Bilde, M., Kerminen, V.-M., and Petäjä, T.: Hygroscopicity, CCN and volatility properties of submicron atmospheric aerosol in a boreal forest environment during the summer of 2010, Atmospheric Chemistry and Physics, 14, 4733-4748, 2014.
Hong, J., Äijälä, M., Häme, S. A., Hao, L., Duplissy, J., Heikkinen, L. M., Nie, W., Mikkilä, J., Kulmala, M., Prisle, N. L., Virtanen, A., Ehn, M., Paasonen, P., Worsnop, D. R., Riipinen, I., Petäjä, T., and Kerminen, V.-M.: Estimates of the organic aerosol volatility in a boreal forest using two independent methods, Atmospheric Chemistry and Physics, 17, 4387-4399, 2017.
Häkkinen, S., Äijälä, M., Lehtipalo, K., Junninen, H., Backman, J., Virkkula, A., Nieminen, T., Vestenius, M., Hakola, H., Ehn, M., Worsnop, D., Kulmala, M., Petäjä, T., and Riipinen, I.: Long-term volatility measurements of submicron atmospheric aerosol in Hyytiälä, Finland, Atmospheric Chemistry and Physics, 12, 10771-10786, 2012.
Jimenez, J. L., Canagaratna, M. R., Donahue, N. M., Prevot, A. S. H., Zhang, Q., Kroll, J. H., DeCarlo, P. F., Allan, J. D., Coe, H., Ng, N. L., Aiken, A. C., Docherty, K. S., Ulbrich, I. M., Grieshop, A. P., Robinson, A. L., Duplissy, J., Smith, J. D., Wilson, K. R., Lanz, V. A., Hueglin, C., Sun, Y. L., Tian, J., Laaksonen, A., Raatikainen, T., Rautiainen, J., Vaattovaara, P., Ehn, M., Kulmala, M., Tomlinson, J. M., Collins, D. R., Cubison, M. J., Dunlea, E. J., Huffman, J. A., Onasch, T. B., Alfarra, M. R., Williams, P. I., Bower, K., Kondo, Y., Schneider, J., Drewnick, F., Borrmann, S., Weimer, S., Demerjian, K., Salcedo, D., Cottrell, L., Griffin, R., Takami, A., Miyoshi, T., Hatakeyama, S., Shimono, A., Sun, J. Y., Zhang, Y. M., Dzepina, K., Kimmel, J. R., Sueper, D., Jayne, J. T., Herndon, S. C., Trimborn, A. M., Williams, L. R., Wood, E. C., Middlebrook, A. M., Kolb, C. E., Baltensperger, U., and Worsnop, D. R.: Evolution of Organic Aerosols in the Atmosphere, Science, 326, 1525-1529, 10.1126/science.1180353, 2009.
Junninen, H., Lauri, A., Keronen, P., Aalto, P., Hiltunen, V., Hari, P., and Kulmala, M.: Smart-SMEAR: on-line data exploration and visualization tool for SMEAR stations, Boreal Environment Research, 2009.
Kim, S., Sinclair, V. A., Räisänen, J., and Ruuhela, R.: Heat waves in Finland: Present and projected summertime extreme temperatures and their associated circulation patterns, International Journal of Climatology, 38, 1393-1408, 2018.

Kontkanen, J., Paasonen, P., Aalto, J., Bäck, J., Rantala, P., Petäjä, T., and Kulmala, M.: Simple proxies for estimating the concentrations of monoterpenes and their oxidation products at a boreal forest site, Atmospheric Chemistry and Physics, 16, 13291-13307, 2016.
Kortelainen, A., Hao, L., Tiitta, P., Jaatinen, A., Miettinen, P., Kulmala, M., Smith, J. N., Laaksonen, A., Worsnop, D. R., and Virtanen, A.: Sources of particulate organic nitrates in the boreal forest in Finland, Boreal Environment Research, 22, 13-26, 2017.
Kourtchev, I., Ruuskanen, T., Maenhaut, W., Kulmala, M., and Claeys, M.: Observation of 2-methyltetrols and related photo-oxidation products of isoprene in boreal forest aerosols from Hyytiälä, Finland, Atmospheric Chemistry and Physics, 5, 2761-2770, 2005.
Kourtchev, I., Fuller, S., Aalto, J., Ruuskanen, T. M., McLeod, M. W., Maenhaut, W., Jones, R., Kulmala, M., and Kalberer, M.: Molecular composition of boreal forest aerosol from Hyytiälä, Finland, using ultrahigh resolution mass spectrometry, Environmental Science and Technology, 47, 4069-4079, 2013.
Kulmala, M., Pirjola, L., and Mäkelä, J. M.: Stable sulphate clusters as a source of new atmospheric particles, Nature, 404, 66, 2000.
Kulmala, M., Vehkamäki, H., Petäjä, T., Dal Maso, M., Lauri, A., Kerminen, V.-M., Birmili, W., and McMurry, P.: Formation and growth rates of ultrafine atmospheric particles: a review of observations, Journal of Aerosol Science, 35, 143-176, 2004.
Kulmala, M.: Build a global Earth observatory, Nature, 553, 21-23, 10.1038/d41586-017-08967-y, 2018.
Liao, L., Dal Maso, M., Taipale, R., Rinne, J., Ehn, M., Junninen, H., Äijälä, M., Nieminen, T., Alekseychik, P., Hulkkonen, M., Worsnop, D., Kerminen, V.-M., and Kulmala, M.: Monoterpene pollution episodes in a forest environment: indication of anthropogenic origin and association with aerosol particles, Boreal Environment Research, 16, 288-303, 2011.
Lim, H.-J., and Turpin, B.: Origins of primary and secondary organic aerosol in Atlanta: Results of time-resolved measurements during the Atlanta supersite experiment, Environmental Science and Technology, 36, 4489-4496, 2002.
Lindinger, W., and Jordan, A.: Proton-transfer-reaction mass spectrometry (PTR–MS): on-line monitoring of volatile organic compounds at pptv levels, Chemical Society Reviews, 27, 347-375, 1998.
Liu, P. S., Deng, R., Smith, K. A., Williams, L. R., Jayne, J. T., Canagaratna, M. R., Moore, K., Onasch, T. B., Worsnop, D. R., and Deshler, T.: Transmission efficiency of an aerodynamic focusing lens system: Comparison of model calculations and laboratory measurements for the Aerodyne Aerosol Mass Spectrometer, Aerosol Science and Technology, 41, 721-733, 2007.
Makkonen, U., Virkkula, A., Mäntykenttä, J., Hakola, H., Keronen, P., Vakkari, V., and Aalto, P. P.: Semi-continuous gas and inorganic aerosol measurements at a Finnish urban site: comparisons with filters, nitrogen in aerosol and gas phases, and aerosol acidity, Atmospheric Chemistry and Physics, 12, 5617-5631, 2012.
Makkonen, U., Virkkula, A., Hellén, H., Hemmilä, M., Sund, J., Äijälä, M., Ehn, M., Junninen, H., Keronen, P., Petäjä, T., Worsnop, D., Kulmala, M., and Hakola, H.: Semi-continuous gas and inorganic aerosol measurements at a boreal forest site: seasonal and diurnal cycles of NH3, HONO and HNO3, Boreal Environment Research, 19 (supp. B), 311-328, 2014.
McGrath-Spangler, E. L., and Denning, A. S.: Global seasonal variations of midday planetary boundary layer depth from CALIPSO space-borne LIDAR, Journal of Geophysical Research: Atmospheres, 118, 1226-1233, 2013.
Pulp and Paper Industry: Paper-, paperboard and pulpmills in Finland: https://www.forestindustries.fi/statistics/pulp-and-paper-industry/, access: January 15 2020, 2018.
Middlebrook, A. M., Bahreini, R., Jimenez, J. L., and Canagaratna, M. R.: Evaluation of composition-dependent collection efficiencies for the aerodyne aerosol mass spectrometer using field data, Aerosol Science and Technology, 46, 258-271, 2012.
Mikhailov, E. F., Mironova, S., Mironov, G., Vlasenko, S., Panov, A., Chi, X., Walter, D., Carbone, S., Artaxo, P., Heimann, M., Lavric, J., Pöschl, U., and Andreae, M.: Long-term measurements (2010–2014) of carbonaceous aerosol and carbon monoxide at the Zotino Tall Tower Observatory (ZOTTO) in central Siberia, Atmospheric Chemistry and Physics, 17, 14365-14392, 2017.
Myhre, G., Samset, B. H., Schulz, M., Balkanski, Y., Bauer, S., Berntsen, T. K., Bian, H., Bellouin, N., Chin, M., and Diehl, T.: Radiative forcing of the direct aerosol effect from AeroCom Phase II simulations, Atmospheric Chemistry and Physics, 13, 1853, 2013.
Ng, N. L., Herndon, S. C., Trimborn, A., Canagaratna, M. R., Croteau, P. L., Onasch, T. B., Sueper, D., Worsnop, D. R., Zhang, Q., Sun, Y. L., and Jayne, J. T.: An Aerosol Chemical Speciation Monitor (ACSM) for Routine Monitoring of the Composition and Mass Concentrations of Ambient Aerosol, Aerosol Science and Technology, 45, 780-794, 2011.
Paasonen, P., Asmi, A., Petäjä, T., Kajos, M. K., Äijälä, M., Junninen, H., Holst, T., Abbatt, J. P., Arneth, A., Denier van der Gon, H., Hamed, A., Hoffer, A., Laakso, L., Laaksonen, A., Leaitch, W. R., Plass-Dülmer, C., Pryor, S. C., Räisänen, P., Swietlicki, E., Wiedensohler, A., Worsnop, D. R., Kerminen, V.-M., and Kulmala, M.: Warming-induced increase in aerosol number concentration likely to moderate climate change, Nature Geoscience, 6, 438, 2013.
Pachauri, R. K., and Meyer, L.: Climate change 2014: Synthesis Report-Summary for Policymakers, Intergovernmetnal Panel on Climate Change (IPCC), Climate change 2014: Synthesis Report-Summary for Policymakers, 2014.

Patokoski, J., Ruuskanen, T. M., Kajos, M. K., Taipale, R., Rantala, P., Aalto, J., Ryyppö, T., Nieminen, T., Hakola, H., and Rinne, J.: Sources of long-lived atmospheric VOCs at the rural boreal forest site, SMEAR II, Atmospheric Chemistry and Physics, 15, 13413-13432, 2015.
Peräkylä, O., Vogt, M., Tikkanen, O.-P., Laurila, T., Kajos, M. K., Rantala, P. A., Patokoski, J., Aalto, J., Yli-Juuti, T., Ehn, M., Sipilä, M., Paasonen, P., Rissanen, M., Nieminen, T., Taipale, R., Keronen, P., Lappalainen, H. K., Ruuskanen, T. M., Rinne, J., Kerminen, V.-M., Kulmala, M., Bäck, J., and Petäjä, T.: Monoterpenes' oxidation capacity and rate over a boreal forest, Boreal Environment Research, 19, 293-310, 2014.
Petit, J.-E., Favez, O., Albinet, A., and Canonaco, F.: A user-friendly tool for comprehensive evaluation of the geographical origins of atmospheric pollution: Wind and trajectory analyses, Environmental modelling and software, 88, 183-187, 2017.
Petäjä, T., Kerminen, V.-M., Hämeri, K., Vaattovaara, P., Joutsensaari, J., Junkermann, W., Laaksonen, A., and Kulmala, M.: Effects of SO2 oxidation on ambient aerosol growth in water and ethanol vapours, Atmospheric Chemistry and Physics, 5, 767-779, 2005.
Pirinen, P., Simola, H., Aalto, J., Kaukoranta, J.-P., Karlsson, P., and Ruuhela, R.: Tilastoja suomen ilmastosta 1981-2010, Ilmatieteen laitos, 2012.
Prăvălie, R.: Major perturbations in the Earth's forest ecosystems. Possible implications for global warming, Earth-Science Reviews, 185, 544-571, 2018.
Ramanathan, V., Crutzen, P., Kiehl, J., and Rosenfeld, D.: Aerosols, climate, and the hydrological cycle, Science, 294, 2119-2124, 2001.
Rantala, P., Aalto, J., Taipale, R., Ruuskanen, T., and Rinne, J.: Annual cycle of volatile organic compound exchange between a boreal pine forest and the atmosphere, Biogeosciences, 2015.
Ridley, D., Heald, C., Ridley, K., and Kroll, J.: Causes and consequences of decreasing atmospheric organic aerosol in the United States, Proceedings of the National Academy of Sciences, 115, 290-295, 2018.
Riuttanen, L., Hulkkonen, M., Maso, M. D., Junninen, H., and Kulmala, M.: Trajectory analysis of atmospheric transport of fine particles, SO2, NOx and O3 to the SMEAR II station in Finland in 1996–2008, Atmospheric Chemistry and Physics, 13, 2153-2164, 2013.
Riva, M., Heikkinen, L., Bell, D., Peräkylä, O., Zha, Q., Schallhart, S., Rissanen, M., Imre, D., Petäjä, T., Thornton, J., Zelenyuk, A., and Ehn, M.: Chemical transformations in monoterpene-derived organic aerosol enhanced by inorganic composition, npj Climate and Atmospheric Science, 2, 2, 2019.
Russell, L. M.: Aerosol organic-mass-to-organic-carbon ratio measurements, Environmental Science and Technology, 37, 2982-2987, 2003.
Saarikoski, S., Mäkelä, T., Hillamo, R., Aalto, P. P., Kerminen, V.-M., and Kulmala, M.: Physico-chemical characterization and mass closure of size-segregated atmospheric aerosols in Hyytiälä, Finland, Boreal Environment Research, 10, 385-400, 2005.
Sarnela, N., Jokinen, T., Nieminen, T., Lehtipalo, K., Junninen, H., Kangasluoma, J., Hakala, J., Taipale, R., Schobesberger, S., Sipilä, M., Larnimaa, K., Westerholm, H., Heijari, J., Kerminen, V.-M., Petäjä, T., and Kulmala, M.: Sulphuric acid and aerosol particle production in the vicinity of an oil refinery, Atmospheric Environment, 119, 156-166, 2015.
Schmidt, A., Leadbetter, S., Theys, N., Carboni, E., Witham, C. S., Stevenson, J. A., Birch, C. E., Thordarson, T., Turnock, S., Barsotti, S., Delaney, L., Feng, W., Grainger, R. G., Hort, M. C., Höskuldsson, Á., Ialongo, I., Ilyinskaya, E., Jóhannsson, T., Kenny, P., Mather, T. A., Richards, N. A. D., and Shepherd, J.: Satellite detection, long-range transport, and air quality impacts of volcanic sulfur dioxide from the 2014–2015 flood lava eruption at Bárðarbunga (Iceland), Journal of Geophysical Research: Atmospheres, 120, 9739-9757, 2015.
Schneider, J., Weimer, S., Drewnick, F., Borrmann, S., Helas, G., Gwaze, P., Schmid, O., Andreae, M., and Kirchner, U.: Mass spectrometric analysis and aerodynamic properties of various types of combustion-related aerosol particles, International Journal of Mass Spectrometry, 258, 37-49, 2006.
Settele, J., Scholes, R., Betts, R. A., Bunn, S., Leadley, P., Nepstad, D., Overpeck, J., Taboada, M. A., Fischlin, A., and Moreno, J. M.: Terrestrial and inland water systems, in: Climate Change 2014 Impacts, Adaptation and Vulnerability: Part A: Global and Sectoral Aspects, Cambridge University Press, 271-360, 2014.
Simon, H., Reff, A., Wells, B., Xing, J., and Frank, N.: Ozone trends across the United States over a period of decreasing NOx and VOC emissions, Environmental Science and Technology, 49, 186-195, 2014.
Sinclair, V. A., Mikkola, J., Rantanen, M., and Räisänen, J.: The summer 2018 heatwave in Finland, Weather, 2019.
Spracklen, D. V., Mickley, L. J., Logan, J. A., Hudman, R. C., Yevich, R., Flannigan, M. D., and Westerling, A. L.: Impacts of climate change from 2000 to 2050 on wildfire activity and carbonaceous aerosol concentrations in the western United States, Journal of Geophysical Research: Atmospheres, 114, 2009.
Stefenelli, G., Pospisilova, V., Lopez-Hilfiker, F. D., Daellenbach, K. R., Hüglin, C., Tong, Y., Baltensperger, U., Prevot, A. S. H., and Slowik, J. G.: Organic aerosol source apportionment in Zurich using an extractive electrospray ionization time-of-flight mass spectrometer (EESI-TOF-MS) – Part 1: Biogenic influences and day–night chemistry in summer, Atmospheric Chemistry and Physics, 2019, 14825-14848, 2019.

Taipale, R., Ruuskanen, T., Rinne, J., Kajos, M., Hakola, H., Pohja, T., and Kulmala, M.: Technical Note: Quantitative long-term measurements of VOC concentrations by PTR-MS – measurement, calibration, and volume mixing ratio calculation methods, Atmospheric Chemistry and Physics, 8, 6681-6698, https://doi.org/10.5194/acp-8-6681-2008, 2008.
Tsigaridis, K., Krol, M., Dentener, F., Balkanski, Y., Lathiere, J., Metzger, S., Hauglustaine, D., and Kanakidou, M.: Change in global aerosol composition since preindustrial times, Atmospheric Chemistry and Physics, 6, 5143-5162, 2006.
Tunved, P., Hansson, H.-C., Kerminen, V.-M., Ström, J., Dal Maso, M., Lihavainen, H., Viisanen, Y., Aalto, P., Komppula, M., and Kulmala, M.: High natural aerosol loading over boreal forests, Science, 312, 261-263, 2006.
Tuononen, M., O'Connor, E. J., and Sinclair, V. A.: Evaluating solar radiation forecast uncertainty, Atmospheric Chemistry and Physics, 19, 1985-2000, 2019.
Turpin, B. J., and Lim, H.-J.: Species contributions to PM2. 5 mass concentrations: Revisiting common assumptions for estimating organic mass, Aerosol Science and Technology, 35, 602-610, 2001.
Wang, K., Dickinson, R. E., Su, L., and Trenberth, K.: Contrasting trends of mass and optical properties of aerosols over the Northern Hemisphere from 1992 to 2011, Atmospheric Chemistry and Physics, 12, 9387-9398, 2012.
Williams, J., Crowley, J., Fischer, H., Harder, H., Martinez, M., Petaja, T., Rinne, J., Back, J., Boy, M., Hakala, J., Kajos, M., Keronen, P., Rantala, P., Aalto, J., Aaltonen, H., Paatero, J., Vesala, T., Hakola, H., Levula, J., Pohja, T., Herrmann, F., Auld, J., Mesarchaki, E., Song, W., Yassaa, N., Nolscher, A. C., Johnson, A. M., Custer, T., Sinha, V., Thieser, J., Pouvesle, N., Taraborrelli, D., Tang, M. J., Bozem, H., Hosaynali-Beygi, Z., Axinte, R., Oswald, R., Novelli, A., Kubistin, D., Hens, K., Javed, U., Trawny, K., Breitenberger, C., Hidalgo, P. J., Ebben, C. J., Geiger, F. M., Corrigan, A. L., Russell, L. M., Ouwersloot, H. G., Vila-Guerau De Arellano, J., Ganzeveld, L., Vogel, A., Beck, M., Bayerle, A., Kampf, C. J., Bertelmann, M., Kollner, F., Hoffmann, T., Valverde, J., Gonzalez, D., Riekkola, M.-L., Kulmala, M., and Lelieveld, J.: The summertime Boreal forest field measurement intensive (HUMPPA-COPEC-2010): an overview of meteorological and chemical influences, Atmospheric Chemistry and Physics, 2011.
Vlachou, A., Daellenbach, K. R., Bozzetti, C., Chazeau, B., Salazar, G. A., Szidat, S., Jaffrezo, J.-L., Hueglin, C., Baltensperger, U., Haddad, I. E., and Prévôt, A. S. H.: Advanced source apportionment of carbonaceous aerosols by coupling offline AMS and radiocarbon size-segregated measurements over a nearly 2-year period, Atmospheric Chemistry and Physics, 18, 6187-6206, 2018.
Zhang, Q., Jimenez, J. L., Canagaratna, M., Allan, J., Coe, H., Ulbrich, I., Alfarra, M., Takami, A., Middlebrook, A., Sun, Y., Dzepina, K., Dunlea, E. J., Docherty, K. S., DeCarlo, P. F., Salcedo, D., Onasch, T., Borrmann, S., Weimer, S., Demerjian, K., Williams, P., Bower, K., Bahreini, R., Cottrell, L., Griffin, R., Rautiainen, J., Sun, J. Y., Zhang, Y. M., and Worsnop, D.: Ubiquity and dominance of oxygenated species in organic aerosols in anthropogenically-influenced Northern Hemisphere midlatitudes, Geophysical Research Letters, 34, 2007a.
Zhang, Q., Jimenez, J. L., Worsnop, D. R., and Canagaratna, M.: A case study of urban particle acidity and its influence on secondary organic aerosol, Environmental Science and Technology, 41, 3213-3219, 2007b.
Zhang, Y., Favez, O., Canonaco, F., Liu, D., Močnik, G., Amodeo, T., Sciare, J., Prévôt, A. S., Gros, V., and Albinet, A.: Evidence of major secondary organic aerosol contribution to lensing effect black carbon absorption enhancement, npj Climate and Atmospheric Science, 1, 47, 2018.
Zhao, D., Buchholz, A., Tillmann, R., Kleist, E., Wu, C., Rubach, F., Kiendler-Scharr, A., Rudich, Y., Wildt, J., and Mentel, T. F.: Environmental conditions regulate the impact of plants on cloud formation, Nature Communications, 8, 14067, 2017.
Äijälä, M., Heikkinen, L., Fröhlich, R., Canonaco, F., Prévôt, A. S., Junninen, H., Petäjä, T., Kulmala, M., Worsnop, D., and Ehn, M.: Resolving anthropogenic aerosol pollution types–deconvolution and exploratory classification of pollution events, Atmospheric Chemistry and Physics, 17, 3165-3197, 2017.
Äijälä, M., Daellenbach, K. R., Canonaco, F., Heikkinen, L., Junninen, H., Petäjä, T., Kulmala, M., Prévôt, A. S., and Ehn, M.: Constructing a data-driven receptor model for organic and inorganic aerosol–a synthesis analysis of eight mass spectrometric data sets from a boreal forest site, Atmospheric Chemistry and Physics, 19, 3645-3672, 2019.

Appendix A: Supporting figures

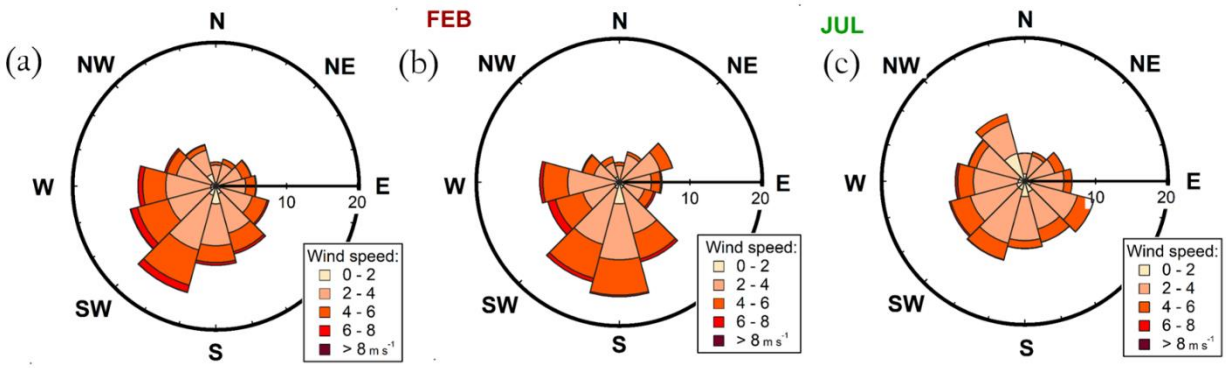

Figure A.1 Wind rose diagrams during the overall measurement period (panel a), February (panel b), and July (panel c). The distance from origin reflects the likelihood of each direction (%) and the color scale reflects the likelihoods of different wind speeds associated with the direction.

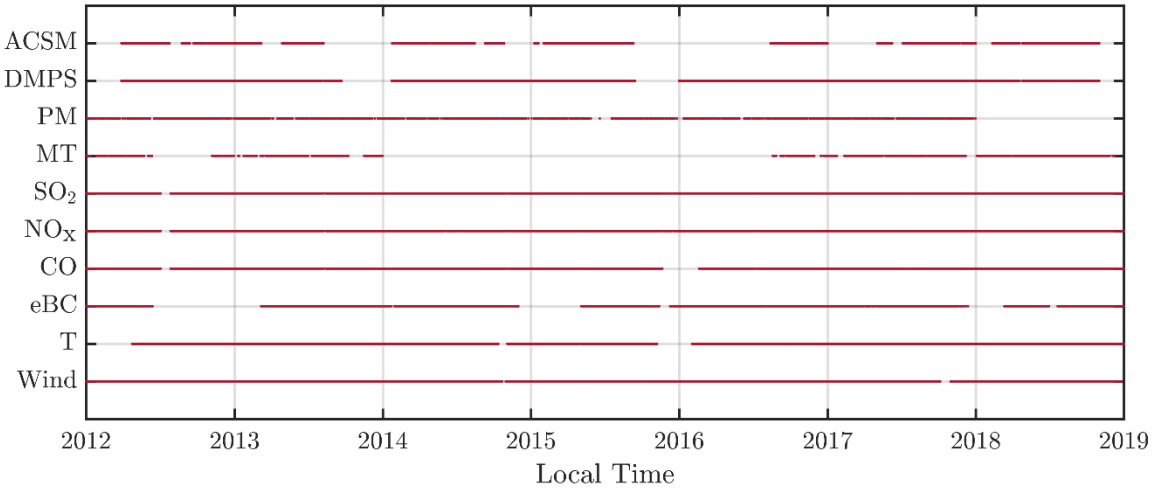

Figure A.2 Data availability during the measurement period. The instrument/measurement parameter is on the y–axis and time is on the x–axis. Gaps in the red line correspond to times when no data was available.

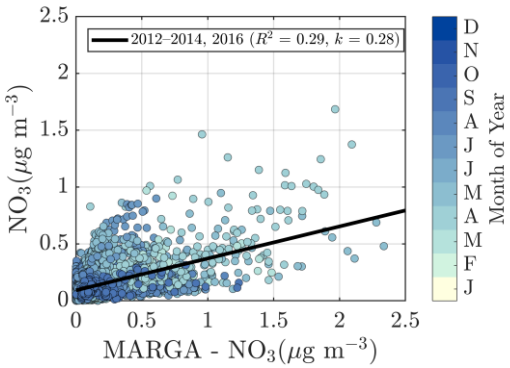

Figure A.3 The ACSM nitrate vs the $PM_{2.5}$ nitrate detected with MARGA–2S. The color coding represents the month of the year. The black line represents the overall linear fit.

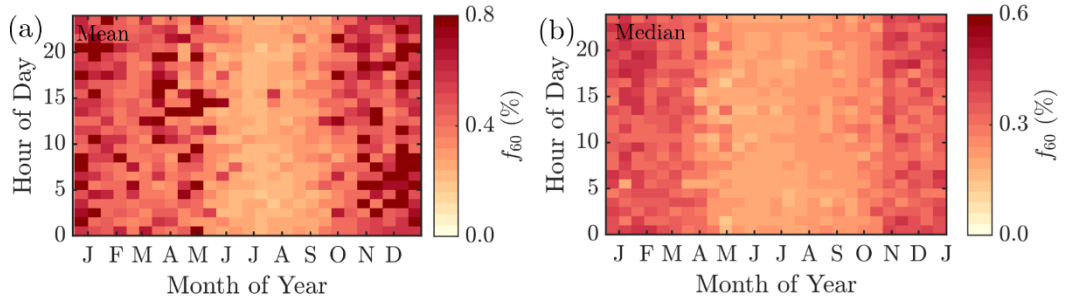

Figure A.4 The mean (a-panel) and median (b-panel) f_{60} (the fraction of m/Q 60 Th signal of the total OA signal) values derived from the ACSM measurements (2012–2018 at SMEAR II). The x-axes represent the time of the year and the y-axes the hour of the day (UTC+2). The coloured pixels represent the f_{60} values. Note the different colour scales between the mean and median figures. It is also worth mentioning that due to the rather low signal to noise ratio of the ACSM, the f_{60} estimates can be very noisy. To avoid the weight of the high and low noise extremes in the a-panel (mean f_{60}), only the range of $0 \geq f_{60} \leq 1$ were included in the f_{60} mean field calculation.

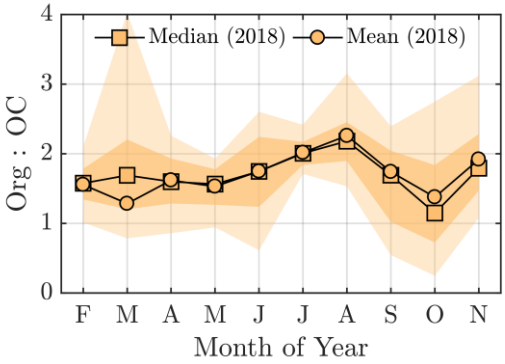

Figure A.5 Organic carbon concentration (OC) vs the organic aerosol concentration (Org) in 2018 at SMEAR II. The darker yellow shadings indicate the area between the 25th and 75th percentiles and the lighter yellow the area between the 10th and 90th percentiles.

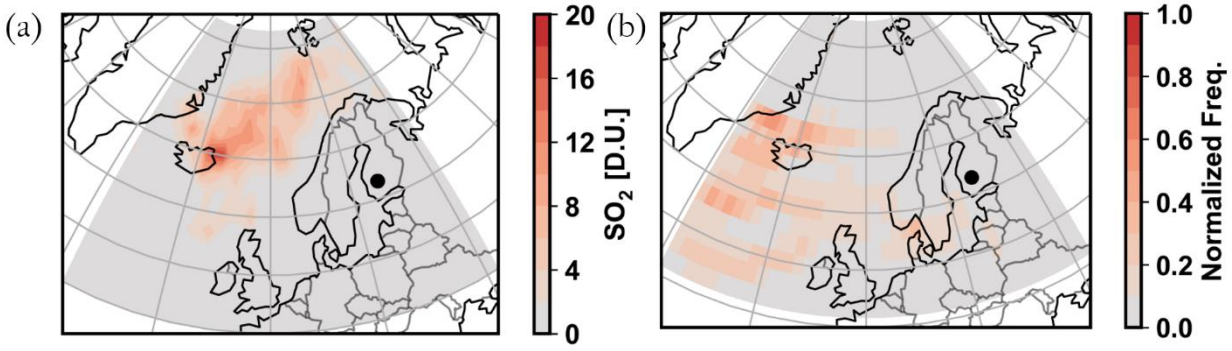

Figure A.6 (Panel a) Average SO_2 concentration in the atmospheric column derived from the ozone monitoring instrument (OMI) aboard Aura satellite for September 2014. High values near Iceland are due to the 2014–2015 flood lava eruption of the Bárðarbunga volcano. (Panel b) 2D normalized histogram of air parcel back trajectories arriving at the SMEAR II station for September 2014. The trajectories are computed using the HYSPLIT model going back 96 hours in time with a resolution of 9 arriving trajectories per hour. Each air parcel path is recorded for each hour. These points are binned in 2 × 2 degree cells. The counting of each cell is then normalized by multiplying it with the square of the distance to the SMEAR II station (black disk marker) in order to highlight the long-range transport patterns.

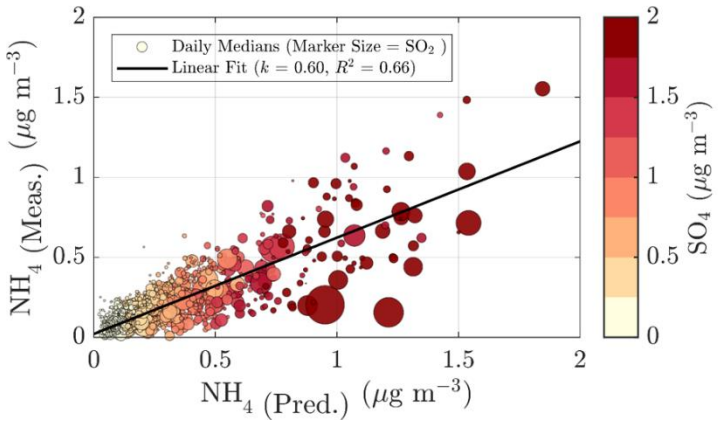

Figure A.7 The relationship between the measured and predicted ammonium concentrations. The marker size reflects the ambient SO_2 concentration and the colour scale sulphate concentration. The linear fit represents the ratio between the measured and predicted ammonium concentration. Drifting from 1 could be linked to more basic or acidic aerosols. The linear fit of 0.66 indicates a possibility of acidic aerosols that decreases in the presence of SO_2. A better acidity approximation could be derived with thermodynamical models.

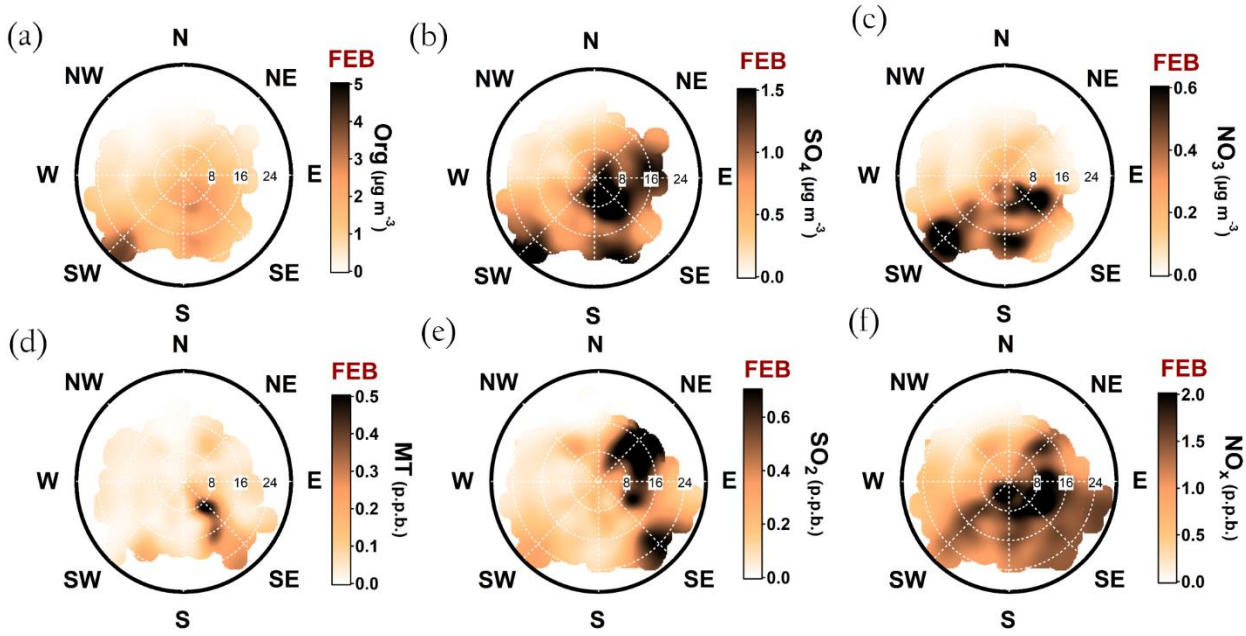

Figure A.8 Openair polar plots for organic aerosol (panel a), sulphate (panel b), nitrate (panel c), monoterpenes (panel d), SO_2 (panel e), and NO_x (panel f) during February. The distances from the origin indicates wind speeds in km h^{-1}. The wind speed grid lines are presented with white dashed circles. The colour scales represent the concentrations observed with each wind speed and direction combinations. As the figures do not indicate any likelihood of the wind speed and distance combinations, Figure A.1 is important to keep in mind while interpreting them. Briefly, N–NE–E is the least probable wind direction, whereas S–SW–W is the most likely. Wind speeds generally stay below 20 km h^{-1}.

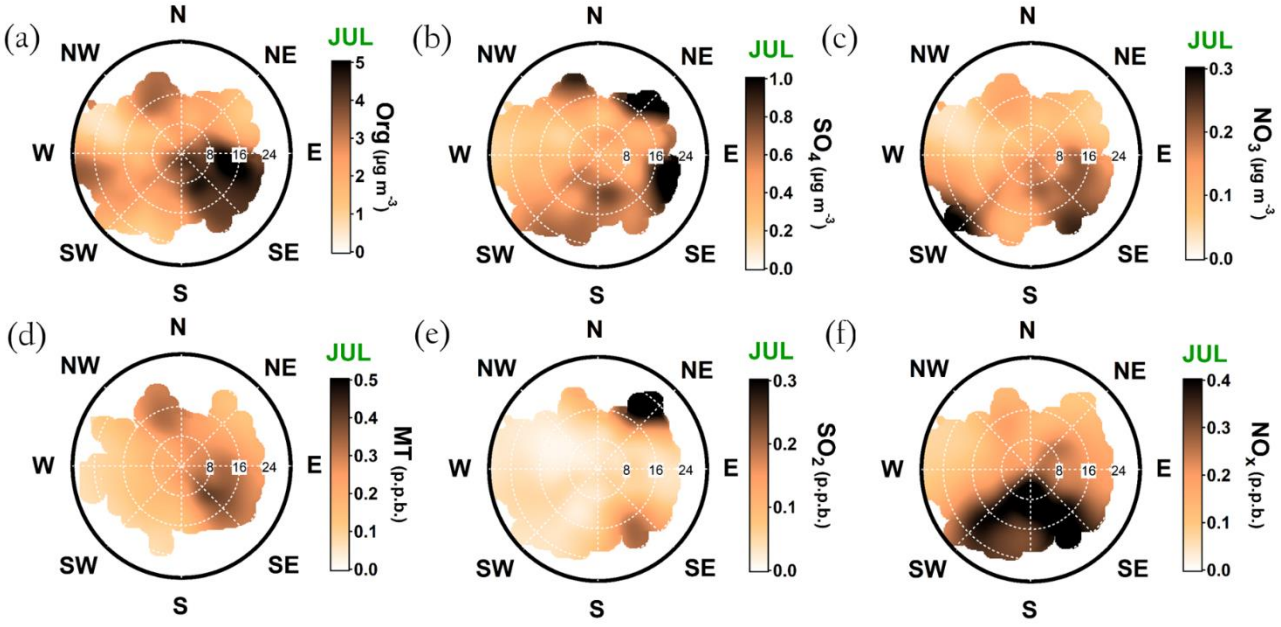

Figure A.9 Openair polar plots for organic aerosol (panel a), sulphate (panel b), nitrate (panel c), monoterpenes (panel d), SO_2 (panel e), and NO_x (panel f) during July. The distances from the origin indicates wind speeds in km h^{-1}. The wind speed grid lines are presented with white dashed circles. The colour scales represent the concentrations observed with each wind speed and direction combinations. As the figures do not indicate any likelihood of the wind speed and distance combinations, Figure A.1 is important to keep in mind while interpreting them. Briefly, N–NE–E is the least probable wind direction, whereas S–SW–W is the most likely. Wind speeds generally stay below 20 km h^{-1}.